UC Riverside

UC Riverside Electronic Theses and Dissertations

Title

Fundamental Studies on the Effects of Microstructure on Thermal Conductivity in Nano-Thermoelectric Materials

Permalink

https://escholarship.org/uc/item/2z70h8gr

Author

Alaniz, Joseph Edward

Publication Date

2013

Peer reviewed|Thesis/dissertation

eScholarship.org

Powered by the California Digital Library
University of California

UNIVERSITY OF CALIFORNIA
RIVERSIDE

Fundamental Studies on the Effects of Microstructure on Thermal Conductivity in Nano-Thermoelectric Materials

A Thesis submitted in partial satisfaction
of the requirements for the degree of

Master of Science

in

Mechanical Engineering

by

Joseph Edward Alaniz

December 2013

Thesis Committee:
Dr. Javier E. Garay, Chairperson
Dr. Guillermo Aguilar
Dr. Lorenzo Mangolini

The Thesis of Joseph Edward Alaniz is approved:

Committee Chairperson

University of California, Riverside

Acknowledgments

The author would like to thank Dr. Sabah Bux and Nasa's Jet Propulsion Laboratory in Pasadena, CA for measuring the thermal conductivity of the samples presented in chapter 6. Drs. Christopher Dames and Zhaojie Wang at UC Berkley are also gratefully acknowledged for their thermal conductivity measurements and guidance throughout the studies presented in this thesis. Finally, Lockheed Martin is gratefully acknowledged for supplying the powders and partial funding for the work presented within this body of work.

Table of Contents

3.2 Densification

Chapter 4: Decoupling the Effects of Grain Size and Porosity in Nano-Grained Silicon

4.3 Results

Chapter 5: Investigation into the Effects of Incomplete Alloying in Silicon Germanium

Chapter 6: Grain Size Distribution- Effects on Thermal Conductivity

List of Figures

List of Tables

Chapter 1: Introduction

As environmental issues surrounding the use of fossil fuels increase, the interest and need for alternative energy sources increases as well. In addition, conventional energy sources waste a significant amount of energy in the form of heat. The common combustion engine, for example, can waste up to seventy five percent of the energy created through burning fossil fuels, leading to an estimated equivalent waste of approximately 200 million gallons of gasoline from light duty vehicles in the US per year [1]. Thermoelectrics are a promising class of material capable of both supplying power to complex systems in remote areas as well as scavenging waste heat from other systems and using it to increase the efficiency of a more conventional system. Thermoelectrics have not been widely put into use, however, due to low efficiencies compared to conventional power systems. Despite significant improvements in material performance as a result of microstructural control, commercial efficiency has seen minimal improvements over the past sixty years.

The majority of thermoelectric material investigations have been focused on property improvement and characterization. Thus rigorous microstructural characterization often does not take a priority. The primary focus of this thesis is to better understand the effects of individual forms of microstructure. Several experimental approaches are shown that are designed to decouple microstructural features and their effects on thermal conductivity. Chapter 2 will provide some basic background information about thermoelectrics and the basic material properties that factor into performance efficiency. These properties will be discussed both in terms of thermoelectric contribution as well as the often adverse effects that they have on one another and how they may be improved using nano-grained materials. Background information will also be provided on the two processes that are used to produce nano-grained materials in these studies: planetary ball milling for preparing powders, and current activated pressure assisted densification (CAPAD) to densify them. Chapter 3 will provide details of the experimental techniques and procedures that were used.

Though most microstructural studies often attribute decreasing thermal conductivity to decreasing grain size, there are often other possible contributing factors such as impurity scattering or more commonly, scattering due to porosity in the material. Chapter 4 details an experiment designed to explore the effects of grain size and porosity separately in order to gain a better fundamental understanding of microstructural effects on thermal conductivity as well as to emphasize the importance of structural characterization when reporting property improvements. The experiment presented here was performed using the CAPAD to densify nominally pure Silicon samples with varying grain sizes and porosity. Thermal conductivity measurements will be presented.

While pure Silicon is an isotropic material in which orientation and alloy scattering is not a concern, high performance thermoelectrics are complex materials in which multiple elements are present. Chapter 5 explores the effects of the degree of alloying in the Silicon Germanium system. Silicon and Germanium are both isotropic materials that form a solid solution at all stoichiometric concentrations. Several ball milling processes are reported in this chapter as well as an analysis of the resulting microstructure. The thermal conductivity of two samples produced with differing powders and microstructures are shown. While the samples reported in this chapter have too many microstructural differences to make any rigorous conclusions, several important trends are shown.

Several of the trends and explanations provided in the Silicon Germanium study are supported by an investigation into the effects of grain boundary distribution presented in chapter 6. This study uses bimodal grain sizes in pure Silicon densified with the CAPAD technique to explore the claim often seen in literature that a larger grain size distribution will lower the thermal conductivity of a material. The studies provided in this thesis set out to explore the effects of microstructure on the thermal conductivity of materials for thermoelectric applications. Many significant improvements have been made in the efficiency of this class of materials, but if these advances are to continue, more microstructural investigations will be needed like the ones presented here.

1.2 References

[1] Z.G. Chen et al. Prog. In Nat. Sci.: Mat. Int. **22** (2012) 535-549

Chapter 2: Background

2.1 Thermoelectrics

Thermoelectrics, a class of materials capable of converting a thermal differential to electrical energy have long been used as an energy source in locations where conventional power supplies are not an option. Satellites [1], lighthouses in Russia [2], and more recently the Mars Rover [3] are all examples in which long term, robust, and reliable power supplies are needed in locations that are difficult or impossible for repairs to be performed. In each of these cases, Radio-isotropic Thermoelectric Generators (RTGs) have proven to be reliable options. More recently, thermoelectrics have been explored as an option for scavenging waste heat from more conventional power sources such as the combustion engine in automobiles [4]. A common thermoelectric module is shown in Figure 2.1a and 2.1b. Many of these modules can be connected in series in order to amplify the effects of the single module and can be used in either power generation mode (Figure 2.1a) or in a Peltier heating/cooling mode (Figure 2.1b).

The efficiency of a thermoelectric material is defined as the figure of merit, denoted as “Z”, which has dimensions T^{-1}. For simplicity’s sake the dimensionless figure of merit is often used, which is the Z of the material multiplied by the temperature at which that efficiency is achieved. This dimensionless figure of merit is known as the “ZT” and is the convention that will be used throughout the rest of this report. The ZT of a material is dependent upon the electrical conductivity (σ), Seebeck Coefficient (S), thermal conductivity (κ) as shown in equation (2.1)

$$ZT = \frac{S^2 \sigma T}{\kappa} \tag{2.1}$$

Each of these material properties plays an important role in the overall efficiency of the thermoelectric material, and they will each be discussed separately in the following sections of this chapter. The thermoelectric efficiency (ε) of the material in power generation mode (as shown in each leg of Figure 2.1a) is given by equation (2.2).

$$\varepsilon = \frac{T_H - T_C}{T_H}\left[\frac{(1+ZT_M)^{1/2}-1}{(1+ZT_M)^{1/2}+(T_C/T_H)}\right] \tag{2.2}$$

T_H is the hot side temperature, T_C is the cold side temperature, and T_M is the average temperature [5]. The first term is the Carnot Efficiency. As can be seen from this equation, the efficiency of a material increases with both an increase in the temperature difference across the material as well as an increase in the figure of merit.

As mentioned earlier in this Chapter, thermoelectric modules can also be used for another important purpose: they can be used as Peltier heaters/coolers (Figure 2.1b). In this mode a current is driven through the module. Because the electric carriers in the two materials can carry differing amounts of thermal energy, the difference in energy must be absorbed from one end and emitted from the other in order to maintain the overall thermal stability of the module [6]. While this function of thermoelectric materials is not the focus of this report, it is an important and common application of thermoelectrics in many industries.

2.1.a Thermoelectric Materials and Properties

Heavily doped semiconductors were well established as the best thermoelectric materials in the 1950s [7]. Electrically insulating materials tend to have a low ZT due to an extremely low electrical conductivity. At the other extreme, metals tend to similarly show low thermoelectric performance due to high thermal conductivities resulting from the added thermal transport by free electrons [8]. As seen in equation 2.1, a high ZT requires a balance of three material properties. A high Seebeck coefficient is required in order to obtain a large voltage response from a given temperature difference, high electrical conductivity is required in order to minimize resistance to the movement of the electrical carriers, and a low thermal conductivity is required to maintain the temperature differential across the material. In the following portions of this chapter, each of these material properties will be discussed along with the often counter-productive effects that they have on the other properties.

2.1.a.i. Seebeck Effect

Johann Sebastian Seebeck discovered that two different metals joined as a loop deflected the needle of a compass when the junctions were exposed to differing temperatures. Initially mistaking this as a thermo-magnetic response, it was eventually learned that the magnetic field was the result of a resulting current produced in the loop. As an approximation, the charge carriers in a material can be considered to behave as atoms in a gas [9]. At thermal equilibrium, the carriers are uniformly distributed throughout the material as shown in Figure 2.2a. When a thermal gradient is applied across the material, the carriers on the hot side have higher energy than the carriers on the cold side and move at a higher frequency and velocity. This means that the electrons on the hot side have a higher likely-hood of migrating toward the cold side, and a carrier concentration gradient forms as shown in Figure 2.2b. As a result of the charge gradient within the material, an opposing voltage forms known as the Seebeck voltage. The measurement of the response that a material will have to a particular temperature difference is characterized as the Seebeck Coefficient (S) as shown in equation 2.3

$$S = \frac{dV}{dT} \tag{2.3}$$

In a thermoelectric material, a high Seebeck coefficient is necessary as it is desirable to have a strong electrical response to a given temperature difference. As seen by the squared term in equation 2.1, the Seebeck coefficient is a significant factor in the thermoelectric figure of merit.

2.1.a.ii Electrical Conductivity

The electrical conductivity (σ) of a material is the measure of a material's ability to pass an electric current. In a given material, the conductivity is dependent upon the number (n) of charge carriers contained within it (e for electrons, h for electron holes) and the mobility of these carriers (μ_e and $\mu_h$for electrons and holes respectively) according to equation 2.4.

$$\sigma = e^{-}(n_e\mu_e + n_h\mu_h) \tag{2.4}$$

e^- is the charge of an electron. In order for a thermoelectric material to function effectively, it is necessary to have a high electrical conductivity so that the movement of the charge carriers produced by the Seebeck response is as unimpeded as possible.

2.1.a.iii. Thermal Conductivity

Thermal conductivity is a measure of a material's ability to transport thermal energy and, as shown in equation 2.5, can be considered as two separate mechanisms.

$$k_{total} = k_l + k_e \tag{2.5}$$

(k_l) and (k_e) are the contributions from lattice vibrations and electrical carriers respectively. As mentioned earlier, metals have high thermal conductivities due to a high contribution from charge carriers. This electrical term is defined by the Wiedemann-Franz law as shown in equation 2.6 in which (L) is the proportionality constant known as the Lorentz number.

$$k_e = \sigma LT \tag{2.6}$$

The lattice conductivity, which will be the main transport property investigated in this thesis, is dependent upon the behavior and movement of vibrations of the crystal lattice

[10]. The characteristics of these vibrations, referred to as phonons, are dependent upon the thermal energy in the material and they show both wave and particle behavior. The lattice contribution to the thermal conductivity of a material can be calculated with equation 2.7,

$$k_l = \frac{1}{3} C_v v_s \Lambda_{tot} \tag{2.7}$$

in which C_v is the volumetric specific heat, $v_s$is the speed of sound in the material, and Λ_{tot} is the mean free path (MFP) of the phonons. The phonon MFP is the distance that a phonon can travel in the lattice before experiencing a scattering event. Though there are many reasons that a phonon may scatter, the three main causes for the materials discussed in this study are impurity scattering, boundary scattering, and umklapp scattering [11]. Impurity and boundary scattering are both caused by discontinuities in the crystal lattice. Impurity scattering is caused by small localized imperfections in the lattice such as imperfections and doping atoms. Boundary scattering refers to the more significant and less localized perturbations in the lattice such as gain boundaries, pores, and surfaces of the material. Boundary scattering will be discussed heavily throughout this report.

Umklapp scattering refers to the scattering of phonons due to other phonons when the sum of the momentum vectors exceeds that of the first brillouin zone. This causes an effective thermal resistance within the material. As the thermal energy and the momentum of the phonons in a material increases, umklapp scattering becomes a significant factor in the total MFP calculation which follows Matthiessen's rule as shown in equation 2.8.

$$\Lambda_{Tot}^{-1} = \Lambda_{imp}^{-1} + \Lambda_{bdy}^{-1} + \Lambda_{umkl}^{-1} \tag{2.8}$$

Λ_{imp}, Λ_{bdy}, and Λ_{umkl} are the respective MFPs as determined by the impurities, boundaries, and umklapp events separately.

As the remainder of this study will contain many plots of thermal conductivity over varying temperature ranges, it is worthwhile to discuss the common shape of the thermal conductivity vs. temperature curve. Figure 2.3 shows the thermal conductivity of single crystal Silicon [12] over a temperature ranging from 10-1600K. To a close approximation, the only terms in equation 2.7 that are temperature dependent are the specific heat and the MFP. The specific heat of a material increases at low temperatures at a rate of T^3 until it approaches the Dulong-Petit limit at which it becomes constant despite increasing temperature. At low temperatures the umklapp scattering is negligible and, based on this simple model, the thermal conductivity should increase with temperature proportionally to the specific heat of the material as shown in figure 2.3a. As the specific heat levels off and becomes constant with increasing temperature, it no longer contributes to increasing the thermal conductivity. This in combination with the onset of Umklapp scattering leads to a leveling off of the thermal conductivity as seen in figure 2.3b. As temperature increases further and Umklapp scattering becomes a major contributing factor, the thermal conductivity begins to decrease as seen in Figure 2.3c. As will be shown in chapter 4, this is only an approximate model that falls short of showing what is actually happening within a material with significant boundary scattering. It does, however, show the common behavior and general shape of a thermal conductivity vs. temperature plot and has been shown to be a useful model when discussing large grain or single crystal materials.

2.1.b. Competing Thermoelectric Properties

Based on the discussion provided in the previous sections, it is often said that the ideal thermoelectric material will have an “electron crystal, phonon glass” type of behavior [13]. This combination of ideal properties is extremely difficult to achieve due to the coupled and often detrimental nature of the thermoelectric properties. As seen in equations 2.5 and 2.6, the thermal conductivity of a material increases with electrical conductivity. In addition, the Seebeck coefficient and the electrical conductivity of a material are inversely related due to filtering of electron energy levels [14].

Due to these competing effects, it is often insufficient to simply improve a single thermoelectric property when attempting to engineer a material with a higher ZT. In order to optimize these materials it is important to obtain a deep and fundamental understanding of how these important properties can be controlled. The focus of this study will be to do so for thermal conductivity.

2.2 Role of Microstructure in Thermal Conductivity

The maximum ZT of thermoelectric materials remained largely unimproved from a value of ~1 until it was suggested that complex nano-structures such as nano-tubes and quantum dots could be used to filter low energy electrons and increase the Seebeck coefficient of these materials [15]. Since then, many high performance materials have been reported [16] and controlling microstructure has become a widely accepted method of improving thermoelectric properties.

Though complex nano-rod and quantum dot materials are efficient thermoelectrics, it is often too costly in both money and time to make usable bulk materials. Nano grained materials have become a topic of intense research due to the relative ease with which they can be densified into bulk materials. The next two sections of this chapter will discuss the effects of nano-grained materials on thermal conductivity as well as some of the places in which our understanding of these effects are incomplete due to difficulties in decoupling the effects of multiple structural features.

2.2.a. Phonon Scattering

As discussed previously, phonons scatter at discontinuities in crystal structures. This can be due to alloying in which the lattice parameter of a host material is distorted by atoms of a secondary material, phase boundaries in which the crystal structure changes to a different structure, the presence of pores in which there are voids of missing atoms (shown in figure 2.4b), and grain boundaries in which the lattice is disrupted over entire planes (also shown in figure 2.4). This behavior can be used to engineer thermoelectric materials with low thermal conductivities as these scattering mechanisms significantly decrease the phonon MFP as shown in equation 2.8 and figure 2.4. This nano-grained approach has been utilized to significantly decrease the thermal conductivity of state of the art thermoelectric materials such as SiGe [17] and Bismuth Antimony Telluride [18]. The commonly used models used to predict these effects of grain boundaries on thermal conductivity predict that the mean free path of materials will equal the grain size in the low temperature regime [19]. The validity of this approximation will be briefly discussed in Chapter 4.

Though the focus of this study will be on the effects of microstructure on the thermal conductivity of materials, it has been shown and is worth mentioning here that simply using porous or nano-grained materials does not necessarily improve the ZT of materials as pores and nano-grains also affect electrical conductivity [20]. Though the electron MFP is significantly shorter than the phonon MFP (a few nanometers for the electron, tens of nanometers to microns for phonons) in silicon and silicon germanium, the ability of the electrons to travel from grain to grain are hindered by the perturbations in the electrical environment of the lattice. This phenomenon is represented in figure 2.5. Table 2.1 shows only a few of the state of the art high performance thermoelectric materials and the approaches used to achieve such high figures of merit.

2.2.b. Decoupling of Microstructural Effects

Much of the focus in thermoelectric research has been on producing high ZT materials and only a few of the many successful examples have been shown in the previous sections of this report. Despite the improvements made, it is difficult to ascertain how much of an impact a single microstructural feature will have on the thermal conductivity of a material. Table 2.2 contains a number of excellent reports on state of the art improvements in thermoelectric performance that contain or could potentially contain multiple features that might contribute to the impressive properties reported within. The focus of the research presented in this thesis is to decouple the microstructural features that affect thermal conductivity so that there is a deeper and more detailed understanding of their individual effects. These details have been difficult to isolate due to the difficulty in controlling different aspects of microstructure during densification of nano-powders. Doing so requires a densification method in which a high degree of control is given over processing temperature, heating rate, processing time, and even the amount of densification the material undergoes. Such a densification method is discussed in the next section.

2.3. Background of the Current Activated Pressure Assisted Densification Technique and Ball Milling

2.3.a. Current Activated Pressure Assisted Densification

Current Activated Pressure Assisted Densification (CAPAD) provides significantly higher densification rates over traditional hot pressing as it uses Joule heating and simultaneous pressure application rather than an external heating element [21]. Often referred to in literature as Spark Plasma Sintering (SPS) or the Field Activated Sintering Technique (FAST), this relatively new method of densification has been shown to be capable of not only densifying materials in a fraction of the time required by traditional sintering techniques but it provides a method to create materials that may be impossible to create otherwise.

When a powder is subjected to high temperatures, mass transport occurs between the powder particles. Six diffusion mechanisms are shown in figure 2.6a-f [22]. Of these mechanisms, (a-c) involve surface diffusion while the others (d-f) are characterized by volume diffusion. The surface diffusion mechanisms, which consolidate the powders but can lead to low density and significant coarsening, require less activation energy and occur at lower temperatures. The Volume diffusion mechanisms, which play a much larger role in densification of the powders, require much higher activation energy and therefore become dominant at higher temperatures. This distinction is where CAPAD is superior to traditional sintering techniques: the higher heating rate of CAPAD significantly reduces the time at which the material is in the regime in which coarsening occurs without densification. This leads to significantly shorter processing times and as a result, it is possible to fully densify materials with little to no grain growth. A more in depth discussion of the inner workings of the CAPAD used in this research are contained in Chapter 3. For more information about the CAPAD technique, it is recommended that readers refer to three recent and extensive reviews of the technique [23,24,25].

2.3.b. Ball Milling

While there are a myriad of ways to make powders with nano-features, the powder processing method used in this body of work will be focused on ball milling. Chapter 5 will describe an attempt to produce a nano-composite with commercial powders through the use of a powder production technique known as planetary ball milling (PBM). This high energy ball milling technique has been used successfully to not only convert powders with large crystals into nano-crystalline powders, but it has also been shown to be capable of simultaneously reacting multiple materials to produce thermoelectric compounds [26]. In several cases, this powder processing method in combination with the CAPAD technique has been used to produce dense state of the art thermoelectric materials.

Ball milling consists of loading powders into a jar along with balls made of a strong material, usually made of the same material as the jar itself. The material comprising the jar and balls is known as the milling media, and must be both a hard and a strong material to prevent deformation and chipping, which could contaminate the powders being milled. While tumble ball milling (TBM) is performed by simply rotating the jar and letting gravity create a tumbling motion that mixes powders with low energy motions and impacts, planetary ball milling is characterized by a different motion that uses centripetal force. This creates high energy grinding and impact forces to mix, break down, and react powders [27]. Figure 2.7 shows a basic schematic of this configuration. This setup consists of a planetary wheel in which the milling media with the powder is inserted. This wheel is at the outer edge of the sun wheel, which rotates independently of the planetary wheel either in the same direction or counter to it. As shown in the schematic, the centrifugal forces in the system cause the balls to move along the inner wall of the jar creating a grinding effect. At a certain point in the rotation, the competing centrifugal forces cancel each other out and the balls enter a ballistic phase in which they leave the wall of the jar and collide with the wall on the other side. This combination creates both thermal and mechanical energy.

While the planetary ball milling technique is capable of creating nano-materials, it can be difficult to alloy certain types of materials. Small particles of softer materials can cold weld together after layering together, while many brittle materials do not react with one another due to the materials breaking apart rather than mixing [28]. Despite these challenges, PBM techniques have been shown to be effective methods of creating nano-grained Silicon-Germanium materials [29]. Details of the PBM used in this body of work will be described in the next chapter.

2.4 Summary

This chapter provided a discussion of the background of thermoelectric materials as well as a description of the important material properties that contribute to thermoelectric efficiency. It was shown that thermal conductivity, electrical conductivity, and the Seebeck coefficient of materials are all interdependent properties making it difficult to design thermoelectric materials without a deep and fundamental understanding of the effects of microstructure on each of these properties. A brief background about Current activated pressure assisted densification and planetary ball milling were provided as these material processing techniques will be heavily used in the following chapters that outline several investigations performed in an attempt to gain a better understanding of the effects of microstructure on the thermal conductivity of thermoelectric materials. Chapter 3 will outline the technical details of how these processing techniques were used in the chapters that follow.

2.5 Figures

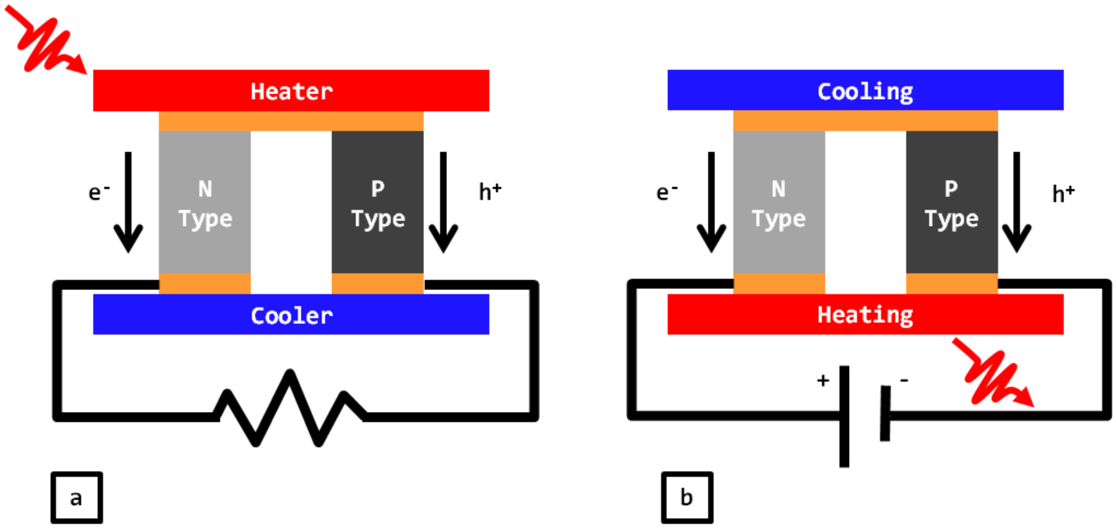

Figure 2.1: A common thermoelectric module made of an n-type and a p-type leg. When subjected to a thermal differential (a) the module can apply an electric current across a load. When a current is applied to the module (b) the module can be used as a Peltier heater/cooler.

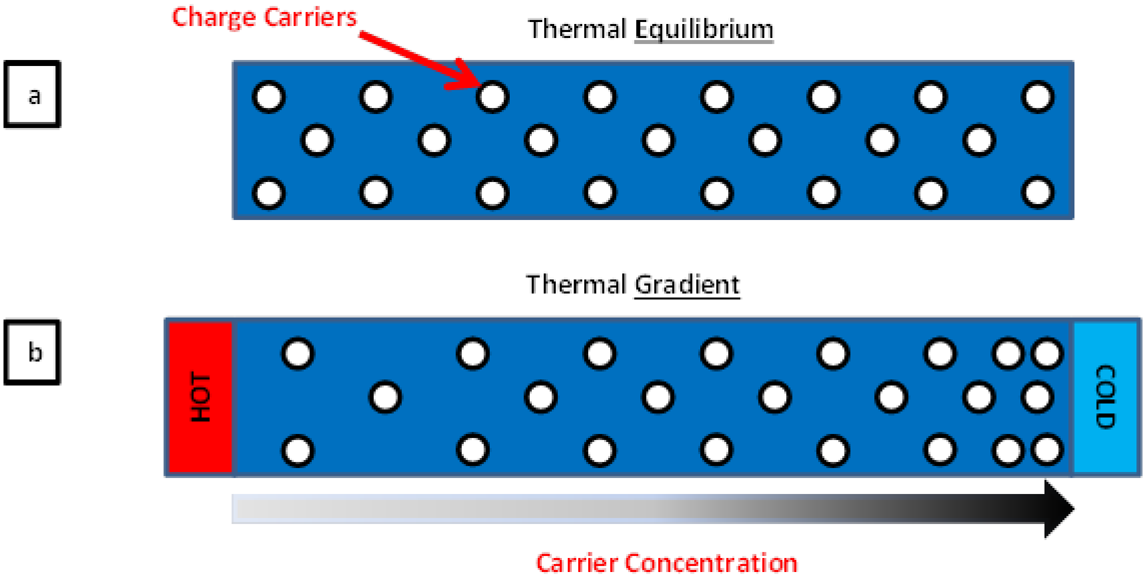

Figure 2.2: Schematics showing the charge carrier distribution in a common semiconductor in thermal equilibrium (a) and subjected to a thermal gradient (b). The carrier concentration gradient shown in (b) is responsible for the Seebeck voltage.

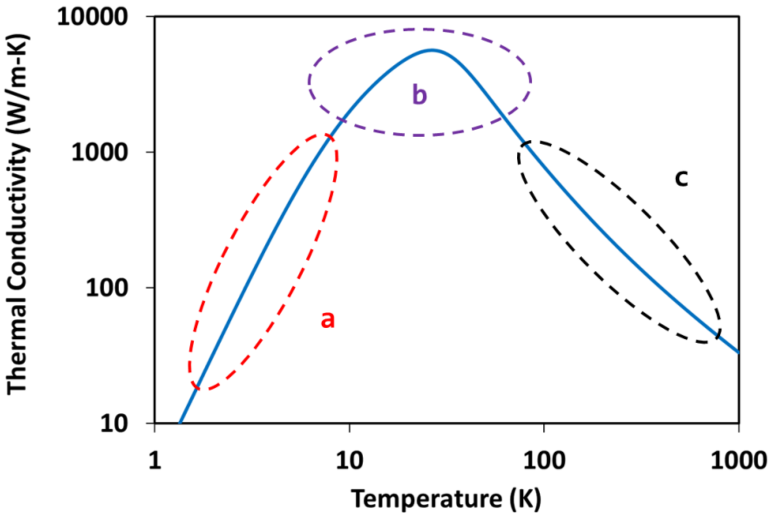

Figure 2.3: Plot of the thermal conductivity of single crystal Silicon [12]. Three important regions are emphasized: the low temperature thermal conductivity is proportional to the Debye T^3 law (a), a transition temperature at which the specific heat becomes temperature independent (b), and at high temperatures umklapp scattering becomes prominent and causes thermal drag.

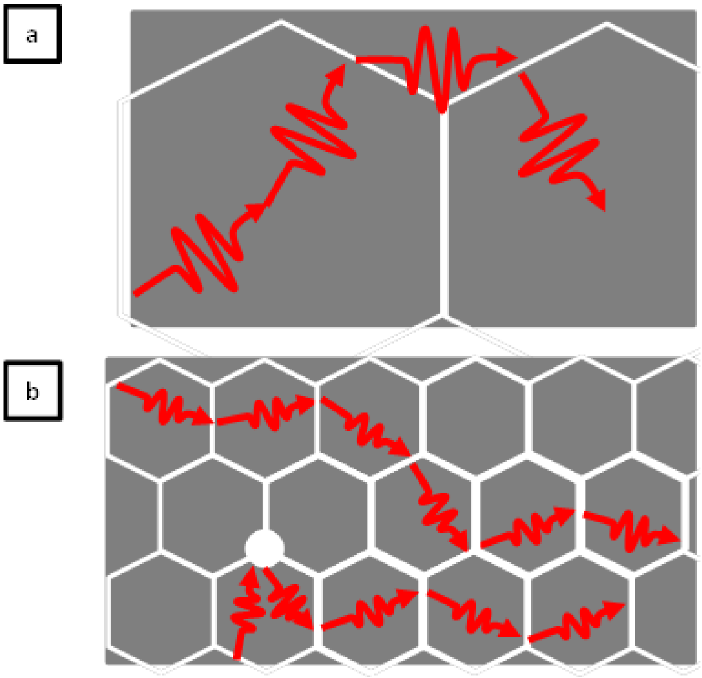

Figure 2.4: Schematic showing phonon behavior in large-grained (a) and nano-grained materials (b). When the phonon mean free path is smaller than the grain diameter (a) the phonons are unimpeded. When the spacing between scattering sites such as grain boundaries and pores is shorter than the mean free path, the MFP is reduced, lowering thermal conductivity.

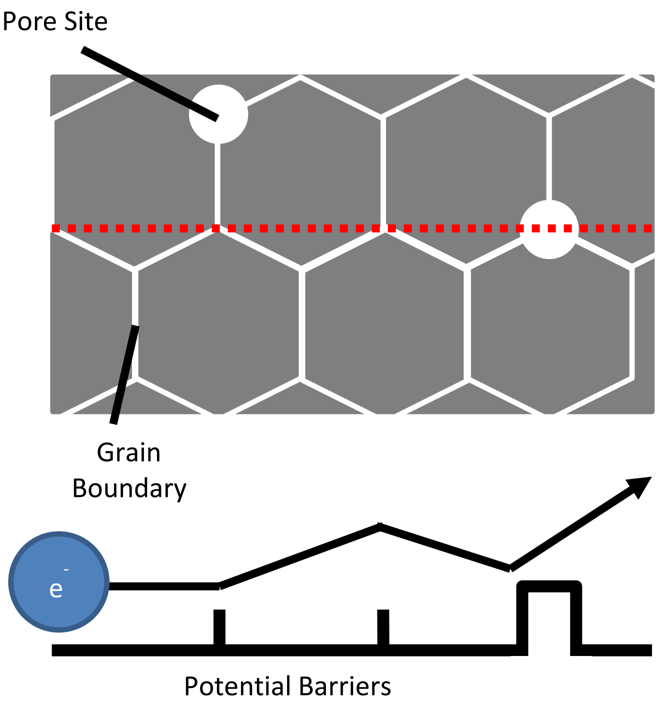

Figure 2.5: Schematic of the movement of an electron across a porous poly-crystalline material. As the electron encounters perturbations in the electronic environment of the crystal it is scattered and its mobility is decreased.

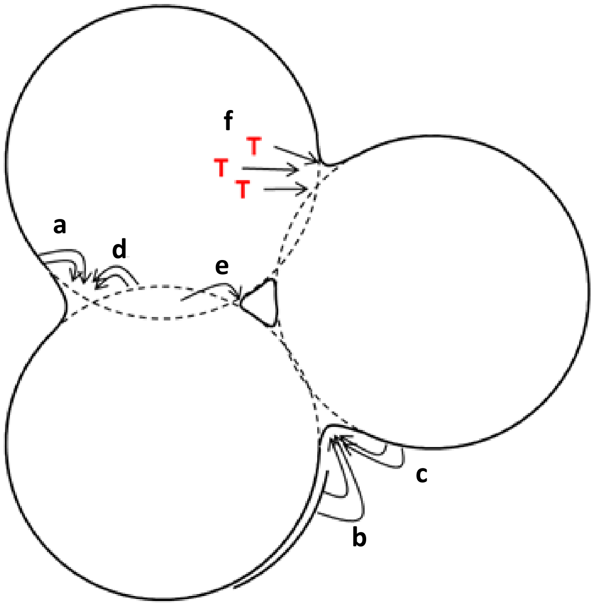

Figure 2.6: Schematic of the mechanisms involved in the diffusion related stages of sintering. Lattice diffusion from the grain surface (a), vapor transport (b), and surface diffusion (c) are primarily responsible for consolidations without densification. Lattice diffusion from the grain boundary (d), boundary diffusion (e), and dislocation diffusion through the lattice are higher temperature mechanisms that contribute to densification of the material.

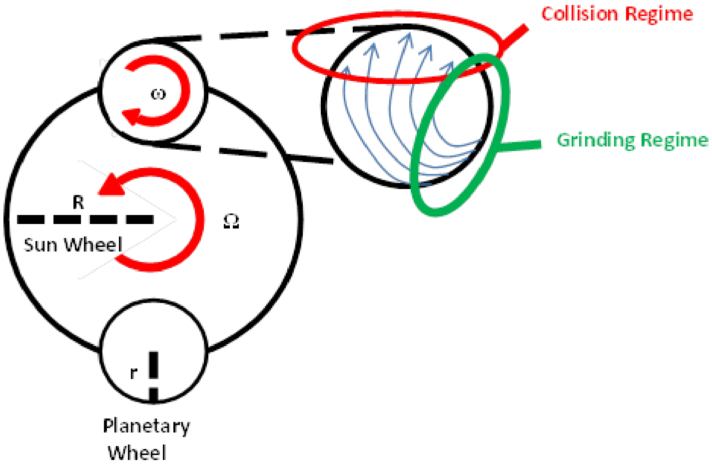

Figure 2.7: Schematic of the planetary ball mill apparatus and the behavior of the balls within the jar on the planetary wheel [expanded area]. The planetary wheel can rotate in either the same or opposite direction as the sun wheel.

Material	Approach Used	ZT (Temp in K)	Reference
p-type Bi_2Te_3/Sb_2Te_3	superlattice	2.4 (300)	30
n-type $AgPb_{18}SbTe_{20}$	nanocomposite	2.2 (800)	31
$PbTe/Pb_{1-x}Eu_xTe$	quantum-dot	2.0 (300)	32
n-type PbSeTe/PbTe	quantum-dot	2.0 (300)	33

Table 2.1: A partial selection of a table presented by Z.G. Chen et al. [34] showing the materials with the four highest ZT materials reported.

Material	Approach Used	Possible Complicating Factors	ZT (Temp in K)	Reference
Si	nano-grain	Density said to "approach 99% density"	0.7 (~1200)	35
n-type SiGe	nano-grain	density not specified	1.3 (1273)	36
p-type SiGe	nano-grain	Dopant presence w/ dopant segregation	0.95 (1073-1173)	17
p-type $Bi_xSb_{2-x}Te_3$	nano-grain	Nano-dots, inhomogeneity, density not reported	1.3 (348-373)	37

Table 2.2: Table of state of the art nano-grained thermoelectrics and the features that make it difficult to discern the effect of grain size alone on the thermoelectric properties.

2.6 References

[1] G. D. Mahan et al. Proc. Natl. Acad. Sci. USA **93** (1996) 7436-7439

[2] W J F Standring et al J. Rad. Prot. **27** (2007) 321

[3] A. Schock et al. Space Nuclear Power Systems **1** (1989) 191-196

[4] S. Kumar et al. J. of Elec. Mat. **42** (2013) 665-674

[5] M. Dresselhaus et al. **19** (2007) 1043-1053

[6] N. Ashcroft, N Mermin. *Solid State Physics*, Brooks/Cole Belmont, CA (1976) pg. 258

[7] M.V. Vedemikov et al. Proc. ICT 98. XVII Int. Conf. on Thermoelectrics (1998) 37-42

[8] G. A. Slack J. Phys. and Chem. of Solids **34** (1973) 321-335

[9] H.P. Myers. *Introductory Solid State Physics,* Taylor & Francis Inc. Philadelphia, PA (1997) pg. 146

[10] D. V. Schroeder. *An Introduction to Thermal Physics*, Addison, Wesley, and Longman. San Francisco, CA (2000) 308-313

[11] C. Dames, Ph. D. Thesis, MIT Dept. of Mech. Eng. (2006) 65-66

[12] Purdue University, Thermophysical Properties Research Center (TPRC). Thermophysical Properties of Matter; Touloukian, Y.S, Ed.; IFI/Plenum: New York, 1970-1979

[13] G.S. Nolas et al. Annu. Rev. Mater. Sci. **29** (1999) 89-116

[14] C. J. Vineis et al. Adv. Mater. **22** (2010) 3970-3980

[15] M.S. Dresselhaus et al. Adv. Mater. **19** (2007) 1043-1053

[16] J. Snyder eta al. Nature Materials **7** (2008) 105-114

[17] G. Joshi et al. Nano Lett. **8** (2008) 4670-4674

[18] B. Poudel et al. Science **320** (2008) 634-638

[19] H. Goldsmid et al. Phys. Lett. A **27** (1968) 523-524

[20] J. H. Lee et al. Nano Lett. **8** (2008) 3750-3754

[21] Z. Shen et al. J. Am. Ceram. Soc. **85** (2002) 1921-1927

[22] Y.M. Chiang, D. P. Birnie, W.D. Kingery, *Physical Ceramics,* John Wiley & Sons, Canada (1997)

[23] J. E. Garay, Ann. Rev. Mat. Res. **40** (2010) 445-468

[24] Z. A. Munir, J. Mater. Sci. **41** (2006) 763-777

[25] R. Orru, Mater. Sci. Eng. R **63** (2009) 127-287

[26] J. Yang et al. Journal of Alloys and Compounds **375** (2004) 229-232

[27] P. Le Brun et al. Mat. Sci. Eng. A **161** (1993) 75-82

[28] C. C. Kock Annu. Rev. Mater. Sci. **19** (1989) 121-143

[29] C. B. Vining, J. Appl. Phys. **69** (1991) 4333-4340

[30] R. Venkatasubramanian et al. Nature **413** (2001) 597-602

[31] K. F. Hsu et al. Science **303** (2004) 818-821

[32] L.D. Hicks et al. Phys. Rev. B **53** (1996) R10493

[33] T.C. Harman et al. Science **297** (2002) 2229-2232

[34] Z. G. Chen et al. Prog. in Nat. Sci.: Mat. Int. **22** (2012) 535-549

[35] S. Bux et al. Adv. Func. Mat. **19** (2009) 2445-2452

[36] X.W Wang et al. Appl. Phys. Lett. **93,** 193121 (2008)

[37] Y. Ma et al. Nano Lett. **8** (2008) 2580-2584

Chapter 3: Experimental Techniques

Chapter 2 provided background information and basic descriptions of a few of the experimental techniques used in this body of work. In this chapter, details of the experimental apparatuses, as well as descriptions of the effects of control mechanisms and parameters for the techniques will be detailed. This chapter will be split into three sections: powder processing techniques, densification techniques, and sample characterization techniques. The following chapters will provide experimental parameters for individual experiments, but for an understanding of the effects of these parameters, the reader should refer back to this chapter.

3.1 Powder Processing

3.1.a Hand Milling

When using either homemade or commercial powders for densification, it is not unusual for the powder to be agglomerated, meaning that multiple grains are grouped together to form a larger consolidated mass. Because the early stages of densification during the current activated pressure assisted densification (CAPAD) technique are dependent upon particle yield and rearrangement, heavily agglomerated powders can lead to porous or low density materials after consolidation [1]. Furthermore, when CAPAD is being used to simultaneously densify and react multiple materials into a single homogenous phase, agglomeration of the original powders as well as insufficient mixing of the powders will often lead to an incomplete reaction due to segregation of the powders. For powders that yield easily or are loosely agglomerated, hand mixing is a good first step toward de-agglomerating the powder.

The method of hand milling used in the work shown in this report was accomplished through the use of a mortar and pestle. In order to maintain uniformity in processing techniques, powders that were hand milled were always treated for ten minutes whether the goal was to break down agglomerates or to mix multiple powders. When a mixture of powders was being produced as for the Silicon Geranium discussed in Chapter 5, the volume of the powder was often too great to mix the whole batch in a single mortar. In this event, the total mixture was broken into smaller batches that were each hand milled for ten minutes. Each of these smaller batches were then mixed together and consequently split into smaller batches again to be hand milled to ensure uniform mixture of the powders.

3.1.b Tumble Milling

Tumble milling, which was mentioned briefly in chapter 2, is a low energy milling technique used to further mix powders that contain more than one single element. This technique consists of placing the powders into a glass jar along with small Zirconia balls which is then placed onto two rotating cylinders. The jar rotates causing the powder and the balls to move up the side until they fall or “tumble” back down to the bottom. This motion mixes the powders for long periods of time. All of the Silicon Germanium powders that utilized tumble milling in this study were milled either overnight or for a full twenty four hours.

3.1.c Planetary Ball Milling

Tumble ball milling is a low energy milling technique that mixes powders but does not impart enough mechanical energy to the powder to alter the microstructure of the material. It also does not create enough thermal energy to cause reactions between multiple elements. As mentioned in chapter 2, planetary ball milling (PBM) is a high energy ball milling technique that uses high rpms to create large amounts of both thermal and mechanical energy. In this technique the powder is subjected to both grinding and collision phenomenon.

The PBM apparatus used in this body of work was a Fritsch Planetary Micro Mill Pulverisette 7 premium line mill. Though other milling media is available, stainless steel jars and balls were used in the studies shown in this report. The PBM technique provides a high degree of control when milling powders, but using this technique is still very much an evolving science. Models based on a few simplifying assumptions have been formulated [2]. The equations estimating the ball velocity and kinetic energy are shown below in equations 3.1 and 3.2.

$$v_b = \left[(W_s R_s)^2 * W_p^2 \left(\frac{R_p - 2R_b}{2}\right)^2 * \left(\frac{1-2W_p}{W_s}\right)\right]^2 \tag{3.1}$$

$$E_b = \frac{1}{2} m_b v_b^2 \tag{3.2}$$

v_b is the velocity of the ball in the jar, W_s and $W_p$are the rotational velocity of the sun wheel and planetary wheel respectively, E_b is the kinetic energy of the ball, and m_b is the mass of the ball. R_s , R_p, and R_b are the radii of the sun wheel, planetary wheel, and the ball respectively. In the Fritsch Pulverisette used in this work, the ratio of the speed of the planetary wheel and the sun wheel is maintained at a constant setting of 2:1 so that the only variables controlled in this setting areW_s,R_b, and m_b. These models are essentially for a single ball in an empty jar and do not represent the values found in reality when the jars contain not only multiple balls but also powder. Table 3.1 shows an example of how the energy of this simplified system can change dramatically by altering only the ball diameter or the rotational speed of the sun wheel. This shows that not only does this system provide a high degree of control over the energy imparted to the powder, but it is also important to carefully select the parameters used for a specific purpose. The specific parameters used in the Silicon Germanium study will be included in Chapter 5.

3.2 Densification

3.2.a CAPAD Specifications

As explained in chapter two, current activated pressure assisted densification (CAPAD) involves simultaneously applying mechanical pressure and heat via internal joule heating to a powder. Figure 3.1 shows a simple schematic of the custom built CAPAD device used for the research presented in this report. The powder of interest is loaded into a die and plunger set (described in detail in the following sections) and pressed between two water cooled electrodes within a custom built, water-cooled, stainless steel vacuum chamber ($<4 \times 10^{-4}$ Torr). Many materials, like the silicon based materials used in this report, form oxides and cannot be processed at high temperatures in an oxygen atmosphere. The following two sections detail the two main variable control structures in this technique: temperature and pressure.

3.2.a.i Temperature Control

The temperature in the system is measured with an n-type thermocouple inserted half way through the thickness of the graphite die and is regulated through an Omega temperature controller. The temperature controller outputs temperature data to a custom built data acquisition program while simultaneously controlling the output of three Xantrex power supplies, each capable of supplying 10 volts and 1200 amps to the electrodes. This system makes it possible to apply heating rates of up to 200^{o}C to the system, achieving temperatures as high as 1200^{o}C in only minutes rather than hours or days as with conventional hot pressing. As discussed in the chapter 2, coarsening mechanisms occur at relatively low temperatures while densification mechanisms are more active at higher temperatures. Because the sample spends so little time at lower temperatures, this densification technique makes it possible to make fully dense samples with little to no grain growth during processing.

3.2.a.ii Pressure Control

While elevated temperatures facilitate the diffusion mechanisms of the latter stages of densification [3], the early stages (particle yield and mechanical rearrangement) are achieved through the application of mechanical pressing. The pressure is applied directly through the electrodes with an Instron test frame (Instron Inc., USA) capable of applying a load up to 150kN. The load, application rate, and hold time are all controlled via a custom Bluehill control program.

3.2.b CAPAD Procedure

The preceding sections described the technical specifications of the CAPAD device and its control systems. While the parameters of each experiment are specifically tailored for the application, the following sections outline the basic procedural steps common throughout each of the experiments.

3.2.b.i Powder loading

Though powder preparation is specific to the desired outcome of the experiment, the loading of the powder is the same for all of the experiments reported in this thesis. Once the powder is prepared, it is loaded into a graphite die and plunger set as shown in figure 3.2. Because all of the materials here are produced with Silicon which reacts readily with Carbon, the materials can react with the die and plungers themselves. In order to protect the graphite components and the sample, the inner surface of the die is wrapped with graphite foil as shown in the photograph in figure 3.2b. The faces of the plungers that come into contact with the powder are similarly covered. Once the die is loaded with powder the entire setup is placed between the graphite heat diffusers on the electrodes of the CAPAD device as shown in figure 3.1. In order to start each experiment under similar conditions and to improve electrical contact between the particles at the start of the experiment, the powder is subjected to a 20kN load for sixty seconds. The load is then decreased back to zero and vacuum is pulled in the stainless steel chamber. At this point the experimental process is dependent upon the material and goals of the experiment and those details will be outlined in the chapters for each experiment.

3.3 Sample Characterization

After densification, the samples are all polished with Silicon Carbide polishing disks down to 1200 grit and then further with Alumina powder to a particulate size of 0.05 microns. This not only removes the carbon deposited on the sample from the graphite paper, but it also prepares the sample for X-ray Diffraction (Bruker D8 Advanced Diffractometer), Secondary Electron Microscopy (Philips XL30 FEG), and for characterization of the thermoelectric properties. The Density of all the samples is measured using the Archimedes method in water.

3.3.a Thermal Conductivity: 3ω method and Laser Flash

There are several common ways of measuring the thermal conductivity of an isotropic bulk material. The two measurement techniques used for characterization in the studies shown are the laser flash method and the 3ω method. The Laser Flash Method involves heating one side of a sample via a laser or flash lamp and using the temperature response on the other side to determine the thermal diffusivity [4]. This process allows the thermal conductivity of the sample to be calculated with prior knowledge of the specific heat and the density of the material. If the specific heat is not known, the thermal conductivity can be measured directly via the 3ω method made popular by David Cahill [5].

In this method a small line heater of known dimensions is patterned onto the surface of the sample using photo-lithography techniques. This heating line, shown in figure 3.3, acts as both a heater and a temperature monitoring device. When an AC current of modulation frequency ω is applied to the heater, the resistance of the line will change with a frequency of 2ω. The voltage of the wire changes with a frequency of 3ω which can then be used to determine the temperature oscillations in the wire as well as the thermal conductivity of the sample itself. The studies discussed in chapters 4 and 5 will include thermal conductivity measurements using the 3ω method performed by Dr. Zhaojie Wang and Prof. Chris Dames (UC Berkley) and the study shown in chapter six will include Laser Flash data performed by Dr. Sabah Bux (Jet Propulsion Laboratory, NASA).

3.4 Summary

The planetary ball milling and CAPAD techniques described in this chapter provide the user with a high degree of control via processing parameters that can be altered for the specific use desired. The experimental chapters 4-6 contain the specific parameters used for each individual study presented in this thesis. This chapter however provides technical specifications of some of the devices used in this work as well as the processing procedures that are common throughout each of the studies shown in this thesis. The following chapters will contain the experimental procedures, results, and analyses used to explore the effects of microstructure on thermal conductivity and will refer back to this chapter when appropriate.

3.5 Figures

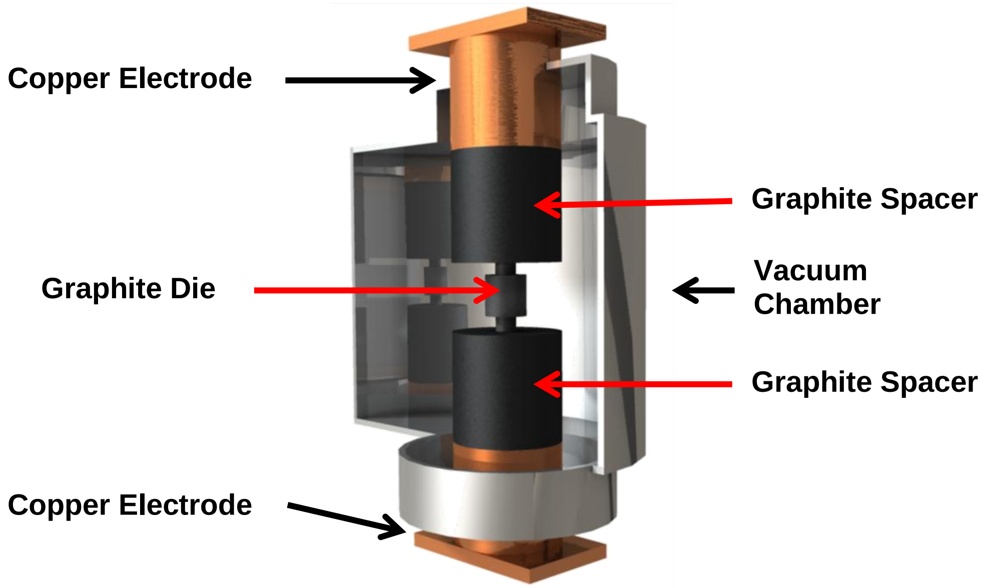

Figure 3.1: Schematic of the custom built current activated pressure assisted densification device used for the investigations presented in this report. The vacuum chamber as well as the copper electrodes is water cooled. Current is passed through the die via the electrodes while an Instron test frame applies compressive force.

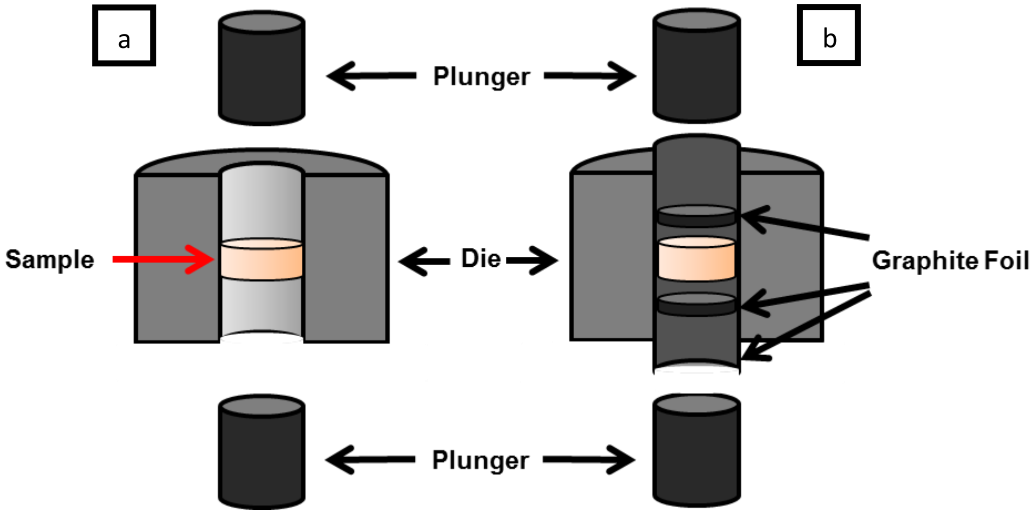

Figure 3.2: Schematic of the graphite die and plunger set with the sample loaded into it (a). For samples that react with carbon, like the Silicon samples presented in this thesis, graphite foil is used to coat the inner diameter of the die and the faces of the plungers as shown in the photograph in (b).

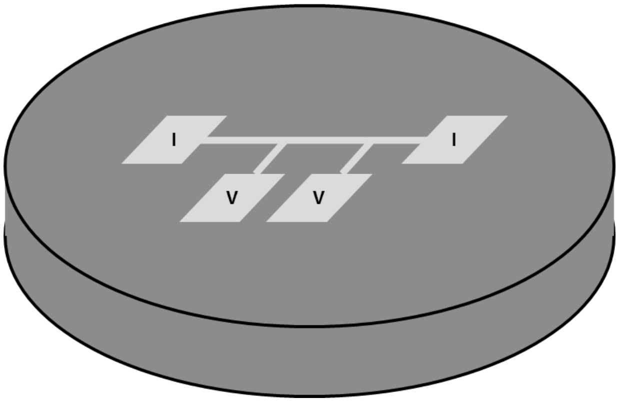

Figure 3.3: Schematic of the pattern printed on the sample for the 3ω thermal conductivity measurement technique.

Ball Diameter (mm)	RPMs	Ball Velocity (m/s)	Ball Kinetic Energy (J)
3.1	300	230	3.27
3.1	**450**	346	7.35
9.3	300	210	79.23

Table 3.1: Calculated ball velocity and kinetic energy within the planetary ball mill derived from equations 3.1 and 3.2, which were taken from reference [2]. The radii of the sun wheel and planetary wheel (R_s and R_p respectively) and the ratio of the rotational frequency of the wheels (W_s and W_p respectively) are dependent on the ball milling apparatus itself while the mass of the ball (m_b) was measured experimentally.

3.6 References

[1] E. J. Felten, J. Amer. Ceram. Soc. **44** (1961) 381-385

[2] N. Burgio et al. Il Nuovo Cimento **13 D** (1991) 459-476

[3] R. Coble, J. App. Phys. **41** (1970) 4798-4807

[4] T. Baba et al. Meas. Sci. Technol. **12** (2001) 2046-2057

[5] D.G. Cahill, Rev. Sci. Instrum. **61** (1990) 802-808

Chapter 4: Decoupling the Effects of Grain Size and Porosity in Nano-Grained Silicon

4.1 Background

As mentioned in chapter 2, the approach of using nano-grains to reduce the thermal conductivity of thermoelectric materials has proven to be a successful way to improve material properties. Despite the significant improvements made, it has been difficult to ascertain the contribution of grain size and density separately from one another. This stems from the difficulty in controlling these features independently from one another during consolidation as well as the fact that a priority has been placed on property investigations over rigorous microstructural investigations.

As a result of these difficulties, many studies report a range of grain sizes, porosities or sometimes do not report these at all. This causes ambiguity in thermoelectric property reports as shown schematically in Figure 4.1a. In order to form a deeper fundamental understanding of the effects of microstructure, it is necessary to decouple these effects and make two sets of samples: one set of samples with a range of densities and a constant grain size, and another set with a wide range of grain sizes with a constant density. This approach is shown in figure 4.1b.

To assure that the observed effects on thermal conductivity can be attributed to the targeted features it is important to select an isotropic material so that preferential orientation is not a consideration. While undoped Silicon is an inefficient thermoelectric material (room temperature ZT=0.01 [1]), its diamond cubic crystal structure makes it an excellent candidate for basic structural studies like the one discussed in this chapter. The powder used in this experiment was a commercial nano-powder provided by

Lockheed-Martin. X-ray diffraction (XRD) of the powder confirmed that the powder was pure within 5 atomic percent while secondary electron microscopy (SEM) showed that it was comprised of ≤ 50 nm grains and agglomerates 10-15 μm wide. The sample with the largest grains was produced with a different commercial powder purchased from Alpha-Aesar with an agglomerate size of 44-150 μm. XRD showed the same level of purity for both powders.

4.2 Procedure

Each sample was produced by loading 1g of powder into the die and plunger set as described in Chapter 3. This is enough material to produce cylindrical samples with a diameter of 19 mm and a thickness of 1 mm. The powder loading and pre-pressing procedure used on each of the samples is described in chapter 3 and each experiment was performed under vacuum at 1.0×10^{-2} Torr. As each experiment was initiated, pressure and temperature were both applied simultaneously. The pressure of all five of the samples shown here underwent a load ramp of 35.3 MPa/min to a maximum of 106 MPa. The sample with full density and the smallest grain size was densified at 1200^{o}C with an initial temperature ramp of 200 ^{o}C/min. It was held at 1200^{o}C for 2.27 minutes to allow for complete densification. This sample was the cornerstone of the study presented in this chapter as it has the smallest grain size of the size distribution samples and the highest density of the density distribution samples. The processing approach for both sets of samples is described briefly in the following sections.

4.2.a Varying Grain Size Samples

Because grain coarsening is a function of temperature, the approach to varying the grain size of a material is straightforward: increasing processing temperature and the amount of time spent at that temperature increases grain size. While the sample with the largest grain size was created using a larger starting powder, the intermediate grain-size sample was created by increasing the processing temperature. The three samples in the varying grain size group were densified at 1200^{o}C, ~1250^{o}C, and ~1250^{o}C (larger starting powder) and were held for 2.27, 2.5, and 1 minute respectively. The hold times for this group were determined based on the estimated time to complete densification as determined by the data returned from the CAPAD device during densification.

4.2.b Varying Density Samples

Based on the information returned from the Instron load frame about the total compression of the system, it is possible to estimate when the powder is undergoing significant densification and when the sample has reached full densification. Based on the information observed from the cornerstone experiment it was possible to monitor the densification behavior of the powder and allow the samples in this group to densify only partially before ending the experiment. The temperatures that the samples reached as the experiments were ended were 1054^{o}C, 1190^{o}C, and 1200^{o}C. No hold times were used to avoid complete densification of the samples except for the cornerstone experiment (1200^{o}C).

4.3 Results

4.3.a Microstructure Characterization

The density and grain sizes of all five samples are shown in the table contained in figure 4.2. The grain sizes of all five samples were determined through direct measurement of the grain diameters of approximately 200 grains/sample. In order to simplify the discussion, the samples will be referred to here in the format: “gain size (relative density)”. For example, the cornerstone sample which had a grain size of 76nm and full density (99%+) will from here on be referred to as the “76(99%)” sample.

The three samples with varying grain sizes were all fully dense and were characterized as 76(99%), 144(99%), and 550(99%). These three samples are shown in the fracture surfaces featured in the SEMs in figure 4.3(a-c). In these images it is apparent that the grain sizes increase with temperature and there is no visible porosity. The SEMs in figure 4.4(a-c) show polished surfaces of the samples with varying density. The porosity of these samples visibly increases and they are characterized as 64(83%), 80(97%), and 76(99%). The grain sizes of these samples are all within ±12 nm of one another.

4.3.b Thermal Conductivity Characterization

The thermal conductivity of the samples with decreasing grain size show significant decreases in thermal conductivity. Figure 4.5 shows thermal conductivity as a function of grain size for multiple temperatures. It is shown that at all temperatures within the measurement range the thermal conductivity decreases with grain size. A similar trend is seen in figure 4.6 in a plot of thermal conductivity vs. porosity (1-% relative density). This figure is a copy of a figure published earlier in a publication about this study [2]. Figure 4.7 shows a plot of the full thermal conductivity curves all on a single graph for easy comparison. All of the curves are significantly below the thermal conductivity of single crystal silicon. At 100^{o}C, the thermal conductivity decreases from 884 to 20.1 W/m-K as the grain size decreases from single crystal to 76 nm. This order of magnitude difference is a result of grain size alone as the density does not change. This graph also shows that as the density of the Silicon decreases by 17%, the thermal conductivity decreases by three quarters of its value. The bubble graph in figure 4.8 shows this data in a different way that shows the progressive change in thermal conductivity as the density and grain sizes change independently. In this graph, both the diameters of the circles as well as their color represent the thermal conductivity of these samples at 300°C. Figure 4.9 shows the thermal conductivity of a select number of samples to show a trend not predicted by the simplistic thermal conductivity model presented in chapter 2: the thermal conductivity increases with a T^2 trend at low temperatures rather than the predicted T^3 trend.

4.4 Discussion

Due to the cubic nature of the crystal structure and the equiaxed shape of the grains shown in figure 4.3, the Silicon samples shown here are expected to show isotropic thermal conductivities. The three varying grain size samples all had densities above 99% meaning that the thermal conductivities reported for these samples are completely independent of density. Each decrease in grain size showed a significant decrease in thermal conductivity indicating that in all of the samples made in this investigation, the mean free path is limited by the grain boundaries. This is in agreement with the fact that the phonon MFP in Silicon is 10-1000nm at room temperature. Figure 4.5 supports this observation.

The dramatic decrease in thermal conductivity with increasing porosity indicates that even a small amount of porosity in a material can have a significant effect on thermal conductivity. It is important to note that both the grain size and the porosity of the silicon samples shown here separately play a significant role in lowering the thermal conductivity. Because of this, the density of thermoelectrics cannot be neglected when reporting the effects of microstructure as is so often done and rigorous microstructural investigation is required before the decreased thermal conductivity of a thermoelectric material is attributed to a particular feature.

Figure 4.6 shows that the thermal conductivity of the porous samples shown here are lower than several models for porous media over the entire temperature range investigated. The models shown here are based on the assumption of spherical, isolated pores with sizes much larger than the phonon MFP [3,4,5]. Figure 4.4 shows that in reality the pores in the samples are non-spherical and are approximately the size of the grain or smaller: significantly smaller than the phonon MFP.

As discussed in chapter 2, the common models for thermal conductivity show a low temperature increase proportional to T^3 which is proportional to the specific heat. As shown in figure 4.9, the samples reported here show a T^2 dependence at low temperatures. Common models for thermal conductivity often make the assumption that $\Lambda_{bdy} = grain\ size$. This model does not account for any frequency dependence of the scattering behavior of the phonons at the grain boundaries. A more accurate model that better describes the behavior observed in this study was developed by Dr. Zhaojie Wang (UCR PhD thesis [6]) and is discussed at length in a published paper based on this work [2]. It presents a model that estimates specular transmission at the grain boundary outperforms the commonly used models. It is recommended that the paper be addressed for more detailed descriptions of the investigation presented here.

4.5 Summary

This chapter outlines the experimental approach taken to decouple the effects of grain size and porosity on thermal conductivity. By using the high degree of control afforded by the Current Activated Pressure Assisted Densification technique two sets of samples were consolidated: one with varying grain size and constant density, and another set with varying density and grain sizes kept approximately the same. The thermal conductivity was significantly decreased by both the grain size and the density separately, indicating that rigorous microstructural characterization needs to be included in any microstructural study of thermoelectrics and their properties. A deeper understanding of the effects of these microstructural features on thermal conductivity was developed as shown in the paper published about this project. A better model accounting for frequency dependent phonon scattering at grain boundaries was formulated for Silicon and it was shown that the current models for phonon scattering at pores underestimate the effects of real porous thermoelectrics.

By better understanding the effects of individual microstructural features on the thermal conductivity of thermoelectric materials, it is possible to better engineer materials for a specific application or desired thermal conductivity. While the focus of this thesis is on the effects of microstructure on thermal conductivity, it is recommended that this approach be extended to the Seebeck coefficient and electrical conductivity. This type of systematic approach would give a strong fundamental concept of how to better engineer thermoelectric materials for improved efficiency. Undoped Silicon lends itself well to this type of study due to its isotropic structure, but it is not an efficient or widely used material for thermoelectric applications. To date, the best thermoelectric materials are all compounds due to complex crystal structure and added alloy scattering effects. The next chapter describes an experiment that explores the effect of the degree of alloying in Silicon Germanium, the most commonly used thermoelectric alloy for high temperature applications.

4.6 Figures

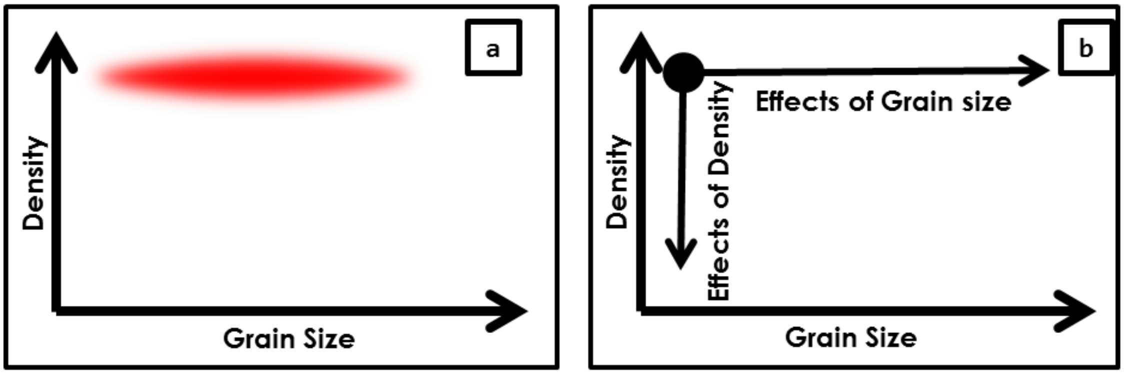

Figure 4.1: Plots representing the ambiguous understanding of microstructural effects on thermal conductivity (a) and the approach for eliminating this ambiguity in the investigation presented in this chapter (b). Two sets of samples will be made: varying density with constant grain size, and varying grain size with constant density.

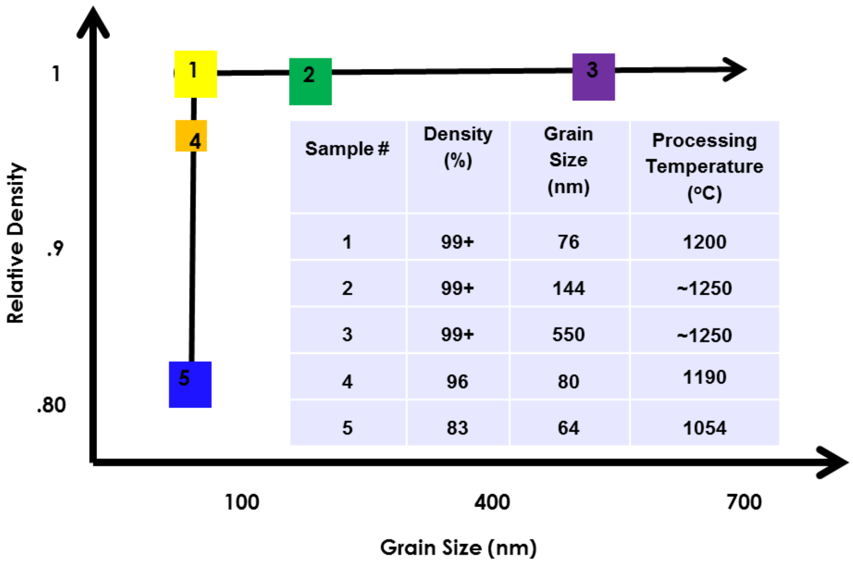

Sample #	Density (%)	Grain Size (nm)	Processing Temperature (°C)
1	99+	76	1200
2	99+	144	~1250
3	99+	550	~1250
4	96	80	1190
5	83	64	1054

Figure 4.2: Plot showing how each of the five samples presented in this study fit into the schematic shown in figure 4.1b. The inset table shows the densities and grain sizes of each of the samples as well as the temperatures at which they were densified.

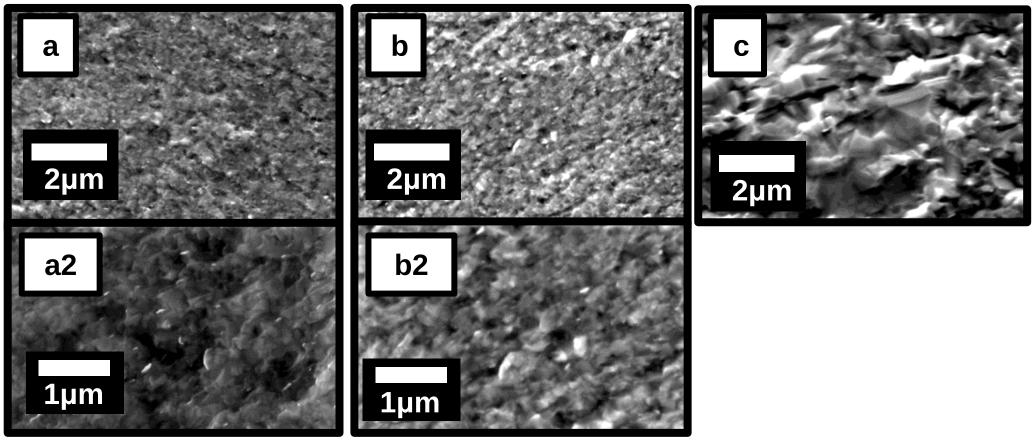

Figure 4.3: Scanning Electron Mircographs of the 76(99%) (a and a2), 144(99%) (b and b2), and the 550(99%) (c) samples. A higher magnification of the 550(99%) is omitted due to the significantly larger grain sizes in this sample.

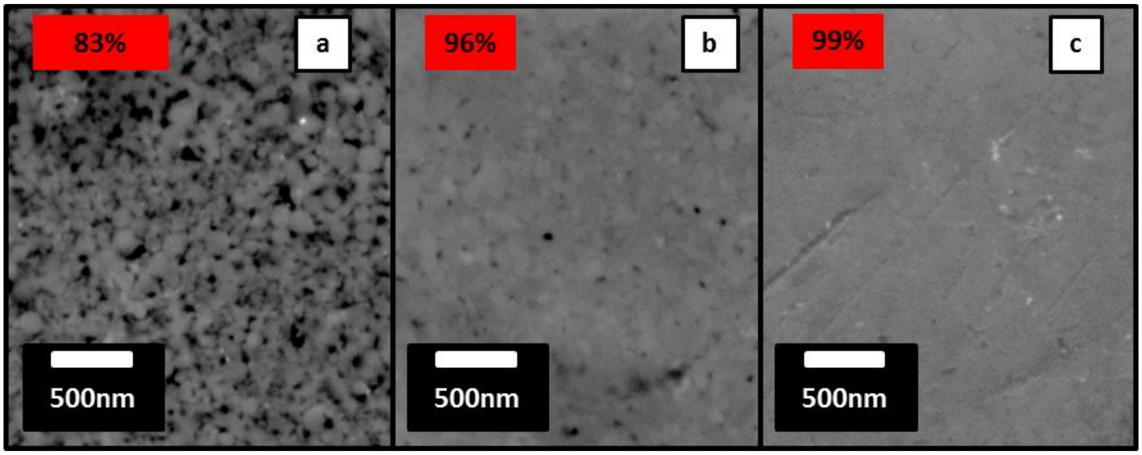

Figure 4.4: Secondary Electron Micrographs of polished surface of the 64(83%) (a), 80(96%) (b), and the 76(99%) (c) samples. The pores of these samples (dark spots) are smaller or comparable to the grain size of the samples and are irregularly shaped.

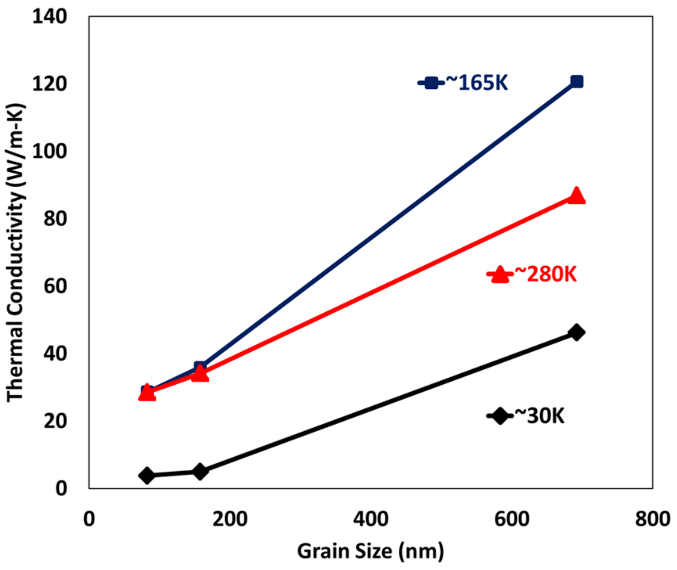

Figure 4.5: Plot of thermal conductivity vs. grain size for selected temperatures. The thermal conductivity increases with grain size over the entire temperature range at all temperatures shown here.

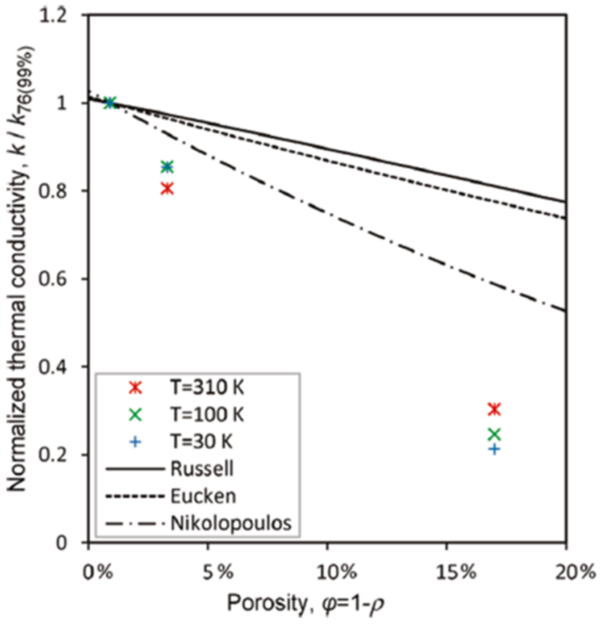

Figure 4.6: Plot of the thermal conductivity (normalized to the 76(99%) sample) vs. porosity for several temperatures of the varying density samples. At all temperatures the effects of porosity are underestimated by Russel [4], Eucken [3], and Nikolopoulos et al. [5]. This plot is copied from a previously published study [2].

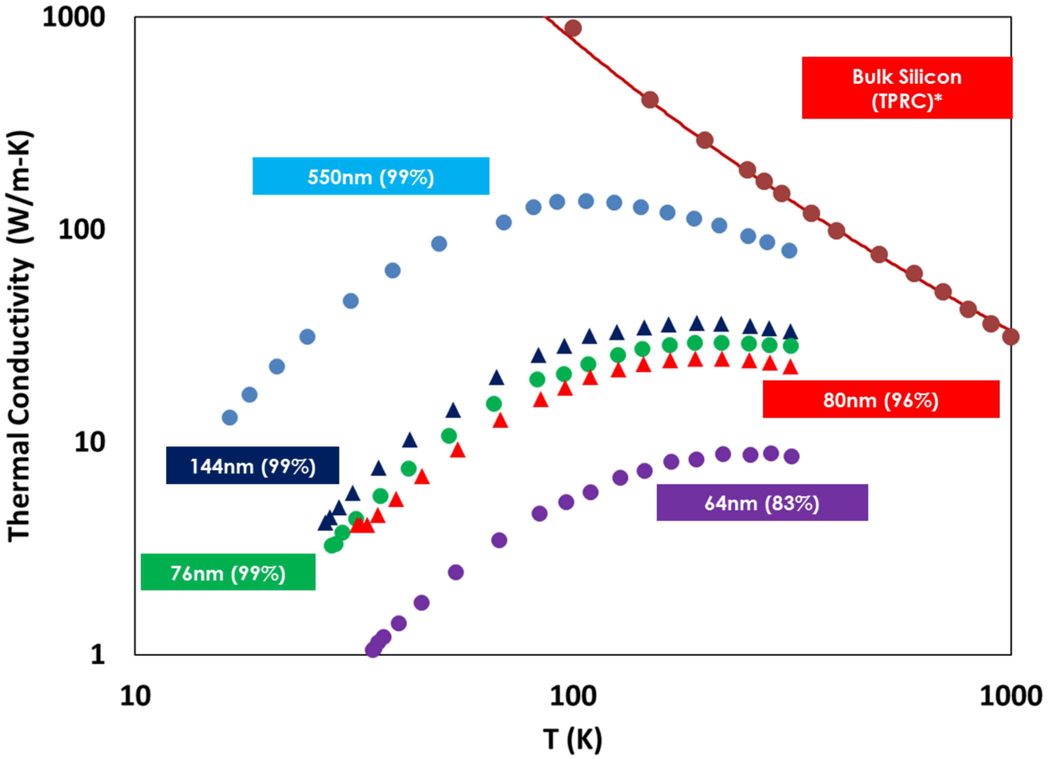

Figure 4.7: Plot showing the thermal conductivity of the five samples over the temperature range measured. For comparison, the literature values of single crystal Silicon is also shown [7].

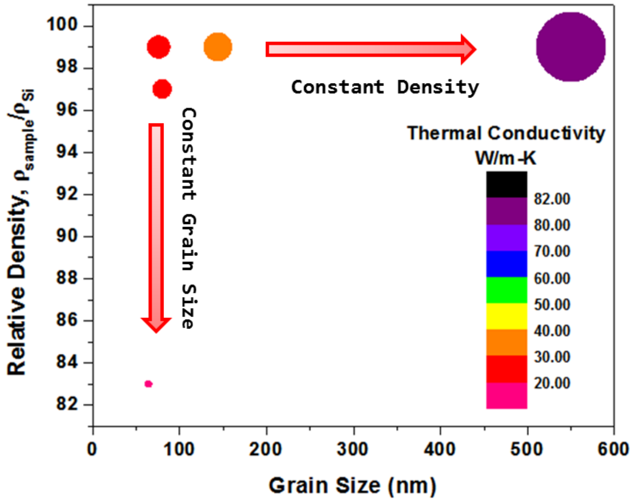

Figure 4.8: Bubble plot of the thermal conductivity vs. grain size and porosity showing that each mechanism independently affects the thermal conductivity.

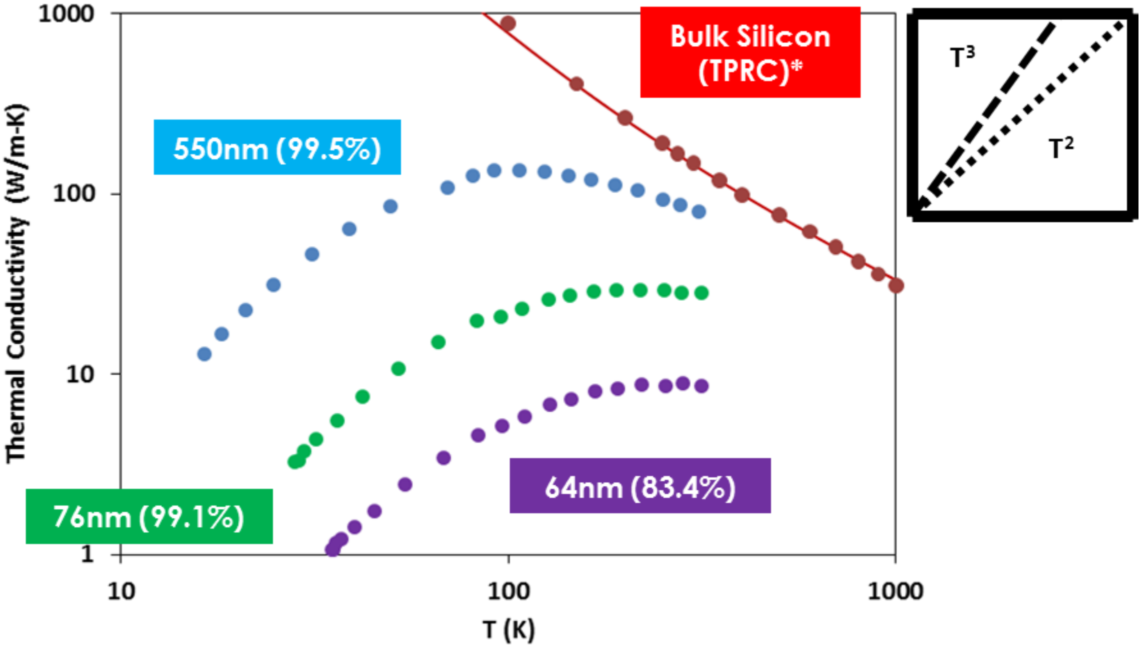

Figure 4.9: Plot of thermal conductivity showing the T^2 behavior of the samples at low temperature. This deviates from the Debye T^3 behavior predicted by most simple models. The literature values of single crystal Silicon is also shown [7].

4.7 References

[1] J.H. Lee et al. Nano Lett. **8** (2008) 3750-3754

[2] Z. Wang et al. Nano Lett. **11** (2011) 2206-2213

[3] A. Eucken, Forsch. Gebiete Ingenieuw (1932) 3

[4] H. W. Russel, J. Am. Ceram. Soc. **18** (1935) 1-5

[5] P. Nikolopoulos et al. J. Am. Ceram. Soc. **66** (1938) 238-241

[6] Wang, Zhaojie. (2012). *Thermal Conductivity of Polycrystalline Semiconductors and Ceramics*. UC Riverside: Mechanical Engineering. Retrieved from: http://escholarship.org/uc/item/06r8376h

[7] Purdue University, Thermophysical Properties Research Center (TPRC). Thermophsical Properties of Matter; Touloukian, Y.S, Ed.; IFI/Plenum: New York, 1970-1979

Chapter 5: Investigation into the Effects of Incomplete Alloying in Silicon Germanium

5.1 Background

Unlike the pure Silicon used to in the previous chapter to show the effects of grain size and porosity on thermal conductivity, all of the state of the art thermoelectric materials to date have been compounds of multiple elements. Alloying can significantly improve thermoelectric performance due to a dramatic decrease in thermal conductivity as a result of phonon scattering as the crystal lattice periodically changes [1]. Silicon Germanium is the most commonly used high temperature thermoelectric material and has a thermal conductivity lower than that of its pure constituents [2].

According to the phase diagram [3], Si and Ge forms a complete solid solution at all stoichiometries (i.e. when Silicon and Germanium are mixed at any concentration they form a solid solution). Both Silicon and Germanium have the same diamond cubic structure, and in a solid solution, neither material has a preferential atomic position: Silicon or Germanium can fill any atomic position in the lattice. Because this structure is maintained at all temperatures below the melting temperature and because it has the same isotropic structure as pure Silicon, Silicon Germanium is an excellent material with which to investigate the effects of phase boundaries without contributing effects from grain orientation. Because alloy scattering has been shown to have such a significant effect on thermal conductivity, and because a systematic investigation of the effects of inhomogeneity in thermoelectric materials has not been performed, an attempt to investigate the thermal conductivity of inhomogeneous nano-composites is presented here. The effects of grain size have been investigated and published elsewhere for

Silicon Germanium, and significant improvements have been made to the efficiency of this already widely used thermoelectric material [4]. The effects of porosity in this material have also been modeled [5].

In an inhomogeneous Silicon-Germanium material, several types of phase boundaries can be present. Because Silicon and Germanium form a solid solution, differing phases can only be formed by regions of the material that are stoichiometricaly different from one another. A schematic of the multiple types of phase boundaries that can be present in the Silicon-Germanium system are shown in figure 5.1(a). Boundaries such as those between homogenous alloys and pure elements (5.1a (i-ii, i-iii)), pure elements of different types (5.1a (ii-iii)), and pure elements to heterogeneous solid solutions (5.1a (ii-iv, iii-iv)) represent inter-granular phase boundaries. Intra-grain boundary scattering is also possible in heterogeneous grains (5.1a (iv)). In this case, the lattice gradually changes, but even this gradient changes the mean free path of the phonons due to altered lattice parameters and bond energy. Though the phases shown are all composed of Silicon, Germanium, or some combination of the two, the lattice parameters of the phases differ leading to phonon scattering at these interfaces.

Because there is often possible ambiguity in the characterization of Silicon Germanium compounds and because the end goal of thermoelectric studies is often fully homogenized materials, microstructural investigations are usually limited to the effects of grain size or porosity as shown in figure 5.2b. While there has been research on these types of microstructural features over a wide range of Silicon Germanium mixtures [4,5,6,7], the research presented in this chapter focuses on a single powder stoichiometry (referred to in this chapter as the “global” stoichiometry) and outlines the approach taken to determine the effect of the degree of homogeneity on the thermal conductivity. Because high efficiency thermoelectrics are multi-component materials, the effects of phase boundaries on the thermal conductivity is an important addition to the fundamental nano-structure studies reported here.

The homogeneity of Silicon-Germanium materials is often established using X-ray diffraction (XRD) and transmission electron microscopy (TEM). While these characterization techniques are widely used, certain limitations can make it difficult to conclusively determine homogeneity. Because Silicon and Germanium both have a diamond cubic structure they both show the same characteristic peaks when using XRD but at different 2θ values due to the difference in the spacing of the atomic planes. Because a solid solution consists of randomly placing atoms of one material into atomic positions of another material, the position of a characteristic peak will shift from the position of one material to the other as the concentration of one material varies in relation to the other [8]. While this effect can give an idea of the concentration of the two present elements, a wide peak can either indicate a small grain size [9] or, as shown later in this chapter, a range of phases with similar compositions. TEM analysis provides a way of imaging the sample and is capable of phase identification, but the sampling area of this form of microscopy is extremely small (often nanometers to hundreds of nanometers) and is insufficient to show inhomogeneities spaced microns apart from one another.   Because of these limitations, the combination of basic XRD and TEM can be insufficient to show homogeneity without extremely tedious and time costly sampling. Secondary electron microscopy (SEM) utilizing back scattering electron (BSE) detection is an excellent way to identify long range inhomogeneities due to the capability to image areas ranging from nanometers to millimeters and the ease with which phase differences can be observed.

Studies of the mechanical alloying of Silicon Germanium have shown that Silicon-Germanium mixtures undergo a number of stages during the alloying process. In the early stage of milling, agglomerates break down followed by fracturing of large grains into smaller grains. Once the crystallites have reached a critical size, mechanical alloying begins due to both mechanical and thermal energy within the milling system. Studies performed using cryogenic conditions have shown that maintaining lower temperatures will decrease the degree of alloying achieved, proving the thermal component of the PBM is an important driving force for alloying [10]. In this chapter, a number of experiments will be shown that show the effect of varying planetary ball milling parameters on the homogeneity of densified Silicon Germanium materials.

5.2 Procedure

Though the stoichiometry of the commonly used Silicon Germanium alloys is $Si_{.8}Ge_{.2}$ these materials can be costly due to the rarity and high price of germanium. In order to minimize the cost of this study, the amount of Germanium was significantly decreased from twenty atomic percent to eight atomic percent ($Si_{92}Ge_{8}$), which is the global stoichiometry of each of the samples shown in this study. Mechanical alloying has become the standard for producing Silicon Germanium alloying with shaker milling and planetary ball milling being the most commonly used methods. One of the benefits to using mechanical milling to create nano-crystalline alloys is that it is possible to use powders with much larger grain sizes. In Silicon Germanium, this is particularly advantageous as nano-crystalline Germanium powders were not commercially available at the time that this report was written. While the nano-silicon powder used in this study was from the same commercial powder used in chapter four, the Germanium powder used in this study was a -100 to +325 mesh powder purchased from Alfa Aesar.

In each of the samples presented here, the powders were first mixed in a mortar and pestle and then via tumble milling as described in chapter 2. This was done to ensure thorough mixing of the constituent powders before high energy ball milling. Consolidation of these powders without PBM was performed using CAPAD at 1100^{o}C, 1150^{o}C, and 1200^{o}C. These samples, as well as all the other samples presented in this chapter were held at temperature for 1100 seconds. This incremental increase in temperature provides the opportunity to observe the effects of temperature on alloying without the added effects of high energy ball milling. In order to explore the effects of high energy ball milling, two samples were prepared by loading the powder into the planetary ball mill with a 20:1 ball:powder weight ratio. These samples were ball milled at 300 rpm in an Argon atmosphere for 6hrs and 12hrs. The powders in these simple alloying studies compacted very easily to the walls of the jar, leading to inefficient mixing and milling of the powders. Because of this observation, the milling procedure was changed to increase the efficiency of the milling.

Because it was observed that a higher Silicon content led to more compaction against the side of the jars, a 90% wt Germanium powder was created with a 40:1 ball:powder ratio at 300rpm for 24hrs. This powder was used as a precursor for the remaining samples reported in this chapter: a small portion of this powder was used as a starting powder and Silicon was added until the global stoichiometry was re-established. Table 5.1 shows a range of processing parameters used in an attempt to vary the homogeneity of the Silicon Germanium alloys. Each of these samples was produced in an argon atmosphere with a ball to powder ratio of 40:1 and were densified via CAPAD in vacuum at 1200^{o}C.

5.3 Results

SEM inspection of the powder subjected to planetary ball milling shows that heavy agglomeration occurs during processing. As shown in figure 5.2a, large agglomerates made up compacted smaller particulates as large as several microns wide form in either loose and rough groups (figure 5.2b) or tight and dense groups (figure 5.2c). The characterization of the samples that underwent no high energy ball milling is presented in figure 5.3 a-c. The data shown in figure 5.3a shows little difference between the three samples with the data of the 1150^{o}C sample and the 1200^{o}C sample look virtually identical. figure 5.3b shows the XRD profile of the [111] peak of the same samples taken with a smaller step size. The smaller step size and longer scan time allows for a better de-convolution of multiple peaks with close to the same 2 theta value. The 1100^{o}C sample shows the partial superposition of two distinct peaks indicating the presence of at least two Silicon Germanium alloys with significantly different stoichiometries. The BSE micrograph in figure 5.3c shows the presence of many bright regions scattered throughout a matrix of a significantly darker material. Electron dispersive spectroscopy (EDS) reveals that both regions contain both Silicon and Germanium, but the darker regions have a much higher concentration of Silicon than Germanium. The brighter regions were shown to contain a significant amount of Silicon, but they also contain a much higher concentration of Germanium. As the densification temperature of the samples increase, the peaks in figure 5.3 a and b come together to indicate that a single phase is being formed, though the peak is still very wide at 1200^{o}C and may be a superposition of two or more peaks that are close enough to one another that they cannot be resolved.

As PBM is introduced, the XRD data (figure 5.4) shows that the peak does not change position but does become narrower. This 2θ peak position corresponds with a Germanium concentration of 0 at%. Figure 5.5 a and b shows BSE micrographs of the samples corresponding to the peaks circled in figure 5.4b. The sample that did not undergo planetary ball milling, shown in figure 5.5a, shows large regions of Germanium rich bright spots compared to the sample that was processed in the planetary ball mill for 12hrs (figure 5.5b). The bright spots in the planetary sample are more numerous but they are significantly smaller. This increased distribution of the Germanium corresponds to the narrowing of the XRD peak.

A combination of SEM and BSE were used to investigate the microstructure of both the Silicon dominant regions and the Germanium rich regions in figure 5.6. The Germanium rich region shown in figure 5.6b shows that these regions consist of large structures that do not appear to be made up of smaller features. These structures are surrounded by large voids and regions of porous large grained material and are isolated from one another by the Silicon dominant regions shown in figure 5.6c. The Silicon dominant regions shown in this micrograph have an average grain size of 196nm.

Of the eight powder batches made with the processing parameters shown in Table 5.1, all of the samples produced with large stainless steel balls (9.28mm diameter) melted at temperatures well between 600-900^{o}C. Of the samples that did not melt, only two samples had enough similarities in processing techniques to compare with one another: portion 2 and portion 4 each were produced with the smaller diameter balls (3.12mm diameter) 450rpms, and were milled in the planetary system for 12hrs and

48hrs respectively. For the remainder of the chapter, portion 2 will be referred to as the 12hr sample and portion 4 will be referred to as the 48hr sample after the processing parameter that sets the samples apart from one another. The BSE micrographs of these two samples are shown in figure 5.7. The 12hr sample shows significant inhomogeneities similar to those shown in the previous samples while the 24hr sample has a relatively high degree of homogeneity.

The thermal conductivity, as measured by Zhaojie Wang via the 3ω method, is plotted in figure 5.8 along with the thermal conductivity of the porous and nano-grained sample (64(83%)) presented in chapter 4 as well as the thermal conductivity of a bulk Silicon Germanium alloy found in literature [11]. This sample has a significantly higher Germanium content than the samples produced in this study. Both sets of reference data have significantly higher thermal conductivities than the samples produced in this study, and the 12hr sample has a higher thermal conductivity than the 48hr sample at all temperatures.

5.4 Discussion

Despite the large regions of inhomogeneity seen is the hand milled and high energy ball milled samples featured in figures 5.3, 5.4, and 5.5, the XRD data shows single peaks for most of them. With the parameters used to perform these XRD measurements, multiple peaks with similar 2θ values convolute and become indistinguishable from one another. Sub-micron grain sizes can also lead to peak broadening making it difficult to attribute the wide peaks shown in this study to phase distribution alone. Because peak broadening is the result of multiple effects, the XRD measurements shown here are insufficient to gauge homogeneity as shown by the inhomogeneous nature of the samples in figure 5.5. In the case of this study, the peaks of the Silicon powder are shifted significantly to the right and the alloying peak appears where the pure Silicon peak is expected. These shifts indicate that the XRD apparatus has not been calibrated and that the peak positions shown in this study cannot be used to qualitatively analyze composition. It is possible that these limitations in the XRD measurements could have been overcome with additional testing, but with the SEM and BSE analysis shown, these extra measures were not necessary.

Similarly, though the samples show regions of homogeneity, the homogenous regions between the Germanium rich features are ~9 micrometers wide. Because TEM analysis typically samples regions only hundreds of nanometers wide, it is possible that TEM would show homogeneity within the samples unless significant time was spent sampling random portions of the sample. This process would be very time intensive, and the BSE process is much more efficient for evaluating these types of long range inhomogeneities.

In the early stages of densification in which particulate deformation and breakdown are dominant, the diversity of agglomerate types shown in figure 5.2 can affect the densification behavior of the powder. The tightly compacted particulates shown in figure 5.2a are likely responsible for the large Germanium rich bright spots seen in the densified samples and featured in figure 5.6. Though the results presented in this study do not lead to a conclusive explanation of the microstructure seen in figure 5.6, a possible explanation is offered here. As the Germanium content of a Silicon Germanium alloy increases, the melting point of the compound decreases [3]. Large Germanium rich agglomerates melting during densification would not only account for the very large features shown in figure 5.6b but it would also account for the void formation and the large amount of growth in Germanium rich grains on the periphery of these features. As partial melting of the Germanium rich material occurs, the rate of diffusion of the Germanium into the silicon rich material increases significantly due to the higher mobility of the viscous or liquid phase. In addition the liquid phase will have high mobility through the grain boundaries, leading to rapid material migration through the grain boundaries of the nano-grained material. This not only leads to void formation due to rapid movement of material, but it also explains the large Germanium rich grains beyond the void region: as the Germanium liquid phase reacts with the Silicon rich region, reaction and material growth occur rapidly causing the grains to not only increase in Germanium concentration but also coarsen rapidly. As the Silicon concentration in the liquid phase increases, it reaches a stoichiometry that is more stable at the high processing temperatures

Because the large Germanium rich regions are microns wide and the regions between them are tens of microns wide, the materials shown in figures 5.3, 5.5, and 5.6 are not nano-composites of the type that can be used for the systematic microstructural study that was originally the goal of this research. The systematic exploration of the effects of the ball milling parameters listed in Table 5.1 were used to attempt to find a processing method that would effectively break down the larger Germanium particulates that are thought to create the large melting features in the bulk and distribute them more evenly throughout the powder. Though the larger balls were used because their larger mass should cause them to have more kinetic energy when they impact the side of the jar, they all caused melting during densification that necessitated ending the experiments early. While the average particulate size of the powder (shown in the final column of the table) was not exclusively larger in the portions made with the larger diameter balls, it is possible that the Germanium rich agglomerates in the powder are larger due to reduced mixing of the powders during ball milling. This may be due to a larger filling volume in the ball milling jar, which is not taken into account in the calculation of ball energy in chapter 2. Because of the difficulties in compositional analysis of individual agglomerates in powder and the destruction of the bulk samples made with these powders, analysis of this explanation is not possible at this time. This explanation also does not address portions 1 and 6, which utilized the smaller diameter balls and still melted.

Two samples that did not melt and only involved the changing of a single milling parameter and provide a chance to explore the effects of the degree of alloying on thermal conductivity: the powders milled in the planetary ball mill for 12hrs and the 48hrs. Because the sample milled for 48hrs is very nearly homogeneous, it represents the extreme end of the spectrum this experiment set out to investigate in that it is a fully homogenized Silicon Germanium nano-alloy. Unfortunately, the sample milled for 12 hours is not the desired partially homogenized nano-alloy this study set out to produce. These two samples will be referenced many times in this study, and will be referred to as the “heterogeneous sample” and the “homogenous sample” for the samples milled for 12 hours and 48 hours respectively. SEM indicates that it still has the voids and the regions of large grain growth seen in previous samples. In addition, the Germanium rich inclusions are 3.9 microns wide and 12 microns apart from one another. The thermal conductivity data shown in figure 5.8 for both the heterogeneous and the homogenous samples are significantly lower than both the lowest thermal conductivity achieved in chapter 4 and the literature value for doped $Si_{.8}Ge_{.2}$. The alloy scattering due to the addition of Germanium accounts for the difference between the samples and the pure Silicon, but the alloy scattering in the literature value should be greater due to a higher concentration of Germanium as well the added effect of the dopants. The lower thermal conductivity of the heterogeneous and homogeneous samples is due to the nano-grained microstructure of our samples compared to the literature material which is described as “bulk”.

Despite the lack of voids and regions of larger grain size in the homogenous sample, the thermal conductivity is 38% lower than that of the heterogeneous sample. It is possible that the germanium rich features in the heterogeneous sample are spaced far enough away from one another that the nano-grained Silicon, which comprises the majority of the sample, dominates the thermal conductivity of the sample. Because the large features in the heterogeneous sample contain higher concentrations of Germanium, the Silicon rich regions contain a lower concentration of Germanium than they would if the sample were homogeneous, and therefore have a lower alloy scattering effect than that seen in the Silicon rich regions of the homogenous sample. As seen in the large difference between the Silicon and the SiGe materials, this difference in alloy scattering can have a significant effect.

5.5 Summary

Because the heterogeneous sample is not a nano-composite, the two samples presented here are insufficient to determine the effects of the degree of alloying on the thermal conductivity of Silicon Germanium nano-composites. It was shown that XRD and TEM analysis may not be sufficient to establish homogeneity of Silicon Germanium alloys unless extraordinary sample measures are taken. SEM with BSE analysis was shown to be an excellent characterization took that is capable of imaging a global indication of material distribution throughout the sample. Of the two samples prepared with similar processing parameters, the more homogeneous sample (the sample that was milled in the planetary ball mill for 48 hrs) had a thermal conductivity of 38% lower than the heterogeneous sample. The thermal conductivity of both samples was significantly lower than that of the pure Silicon sample shown and the coarse grained material shown from literature. The microstructure shown in the heterogeneous sample indicates that planetary ball milling may be an insufficient method with which to process the Silicon Germanium powders to form evenly distributed inhomogeneous Silicon Germanium nano-composites. Due to the incomplete mixing of the Silicon and Germanium powders evidenced in the samples shown here, it is recommended that alternative powder sources and processing techniques are used to complete this study. If a nano-Germanium powder source is found that has little agglomeration and a more efficient mixing technique is used to more evenly distribute the Germanium powder, it is likely that the alloying of these composites can be controlled more systematically. It remains to be shown that it is possible to produce a stable nano-composite in which the Silicon and the Germanium do not alloy at high temperatures.

5.6 Figures

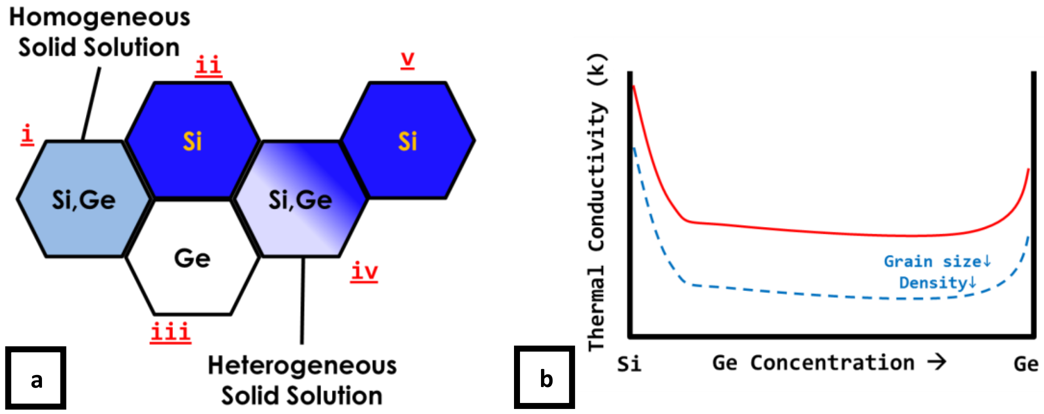

Figure 5.1: Schematic of the multiple types of phase boundaries that can be present in the Silicon-Germanium system (a). Boundaries such as those between homogenous alloys and pure elements (i-ii, i-iii), pure elements of different types (ii-iii), and pure elements to heterogeneous solid solutions (ii-iv, iii-iv) represent inter-granular phase boundaries. Intra-phase boundary scattering is also possible in heterogeneous grains (iv). Other investigations have focused primarily on the effects of grain size or porosity on the material properties of homogenous solid solutions as shown in the illustration in (b).

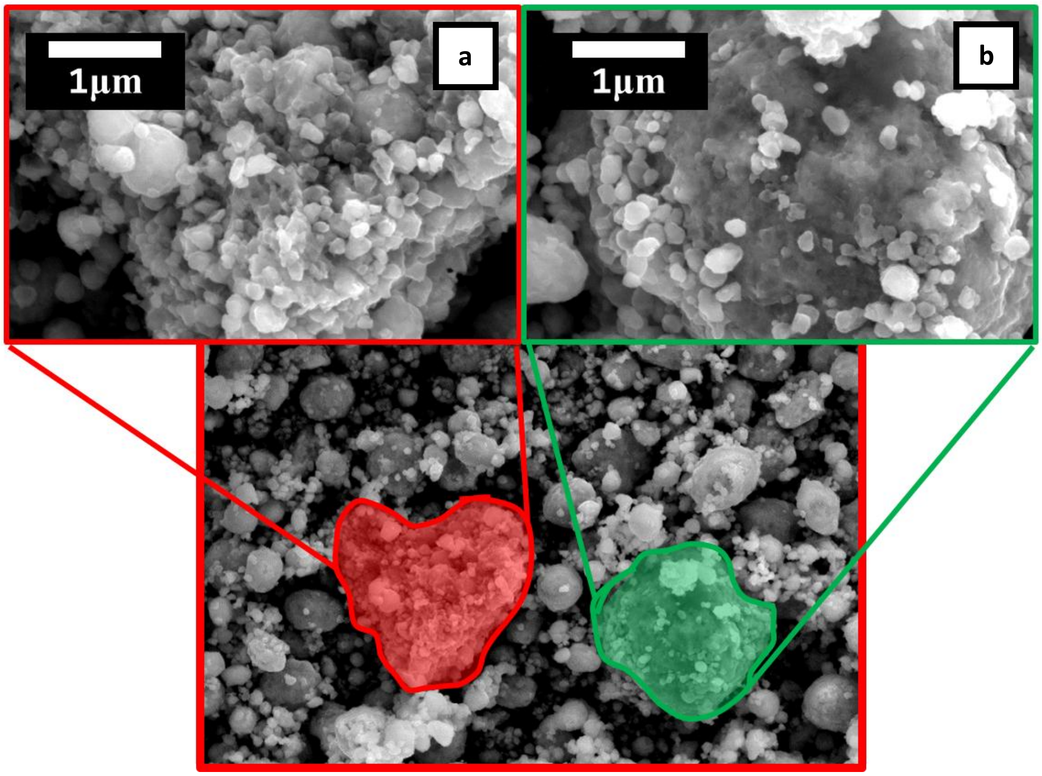

Figure 5.2: Micrograph of 90 wt% powder after 24hrs of planetary ball milling. The Blown up areas show agglomerates of two distinct types: loose particulates of low density (a) and particulates comprised of dense groups (b).

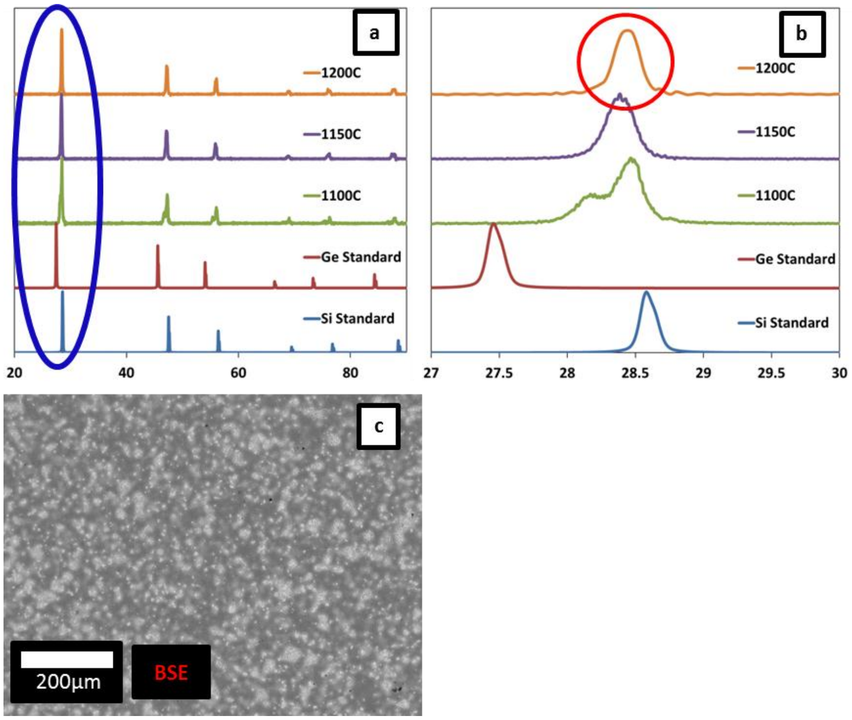

Figure 5.3: X-ray diffraction plot (a) of samples produced through hand mixing and tumble mixing and subsequently densified at 1100, 1150, and 1200°C. The circled peaks are shown in greater detail (b) for easier interpretation of the multiple peaks shown in the 1100°C sample. The Backscattering micrograph of the 1200°C shows significant regions of inhomogeneity despite the single peak shown in (b).

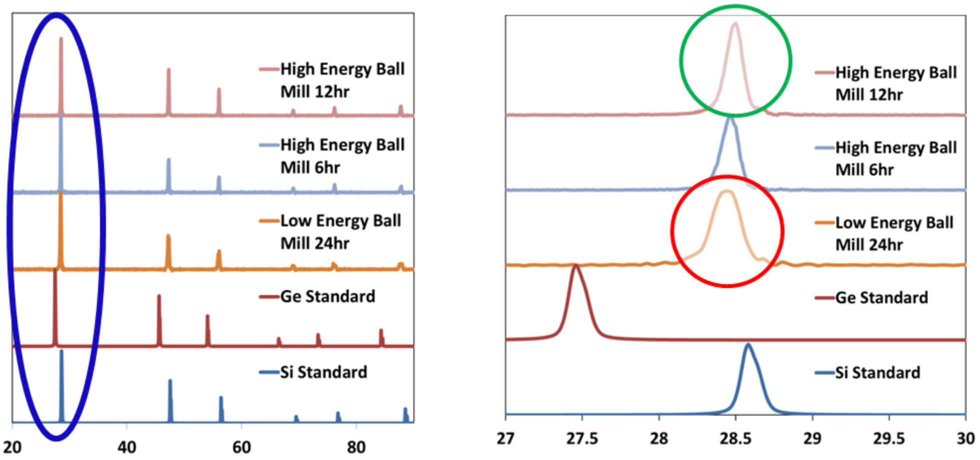

Figure 5.4: X-ray diffraction plot comparing the 1200°C tumble milled sample with the samples produced from planetary ball milling (a). The circled peaks are expanded (b) to show the narrowing of the primary peak. Micrographs of the circled samples in (b) are shown in Figure 5.5

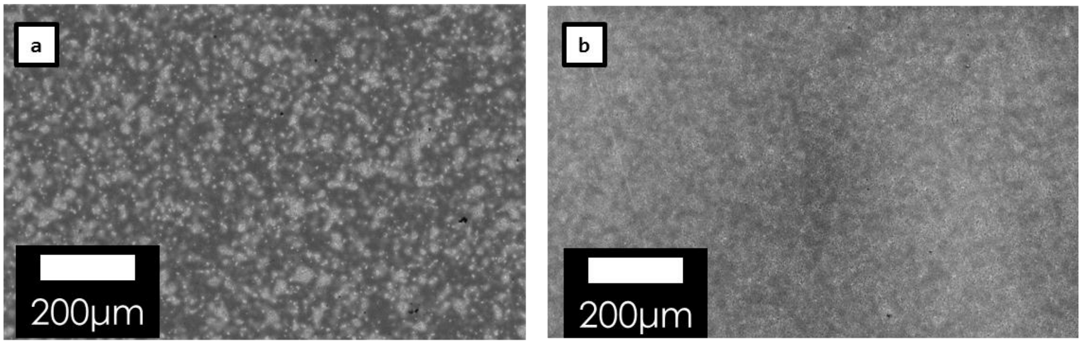

Figure 5.5: Backscattering electron micrographs of the samples planetary ball milled as 20 wt% powders for 12hrs (a) and 24hrs (b).

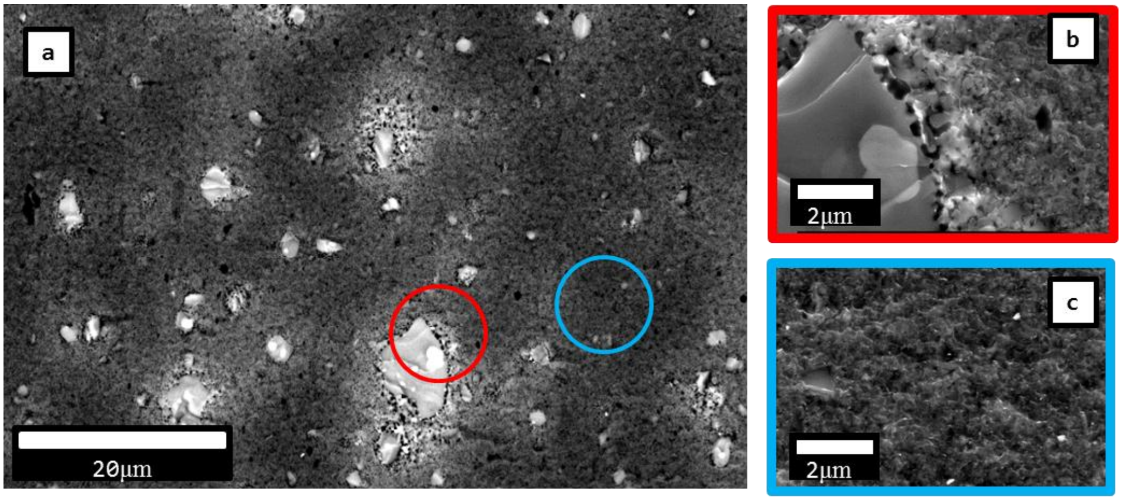

Figure 5.6: Backscattering Electron micrograph (a) showing a higher resolution image of the inhomogeneities of a sample made with an initial 60 wt% powder. The magnifications of the two circled regions are scanning electron micrographs of the germanium rich region (b) and the silicon dominated region (c).

	Ball Size	RPMs	Mill Time (hrs)	Particulate Size (microns)
Portion1	Small	300	24	4.3
portion2	Small	450	12	4.79
portion3	Large	450	12	6.43
portion4	Small	450	48	5.37
portion5	Large	450	24	5.63
portion6	Large: Small	450	12:12	5.46
portion7	Small	300	100	4.87
portion8	Large	300	100	4.85
Small Balls= 3.12mm			**Large Balls= 9.28mm**	
	Melt		**No Melt**	

Table 5.1: Processing parameters and results of the experiments attempted using the 90 wt% precursor powder. Particle sizes indicated were measured through visual inspection via optical microscope.

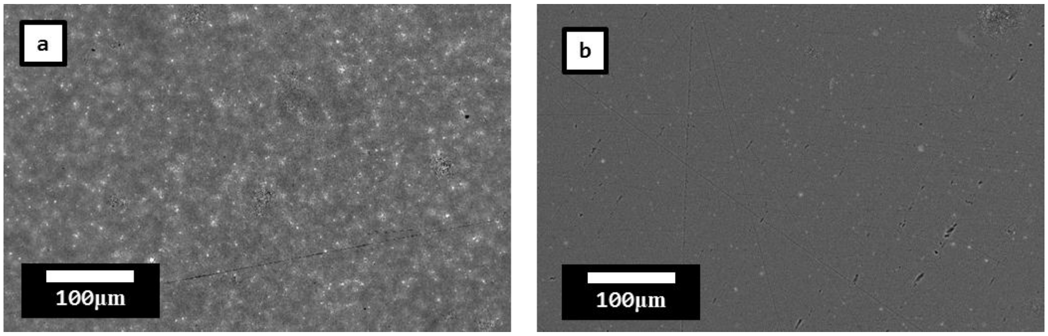

Figure 5.7: Backscattering electron micrographs of the heterogeneous (a) and the homogeneous (b) samples densified from powder portions 2 and 4 (Table 5.1) respectively.

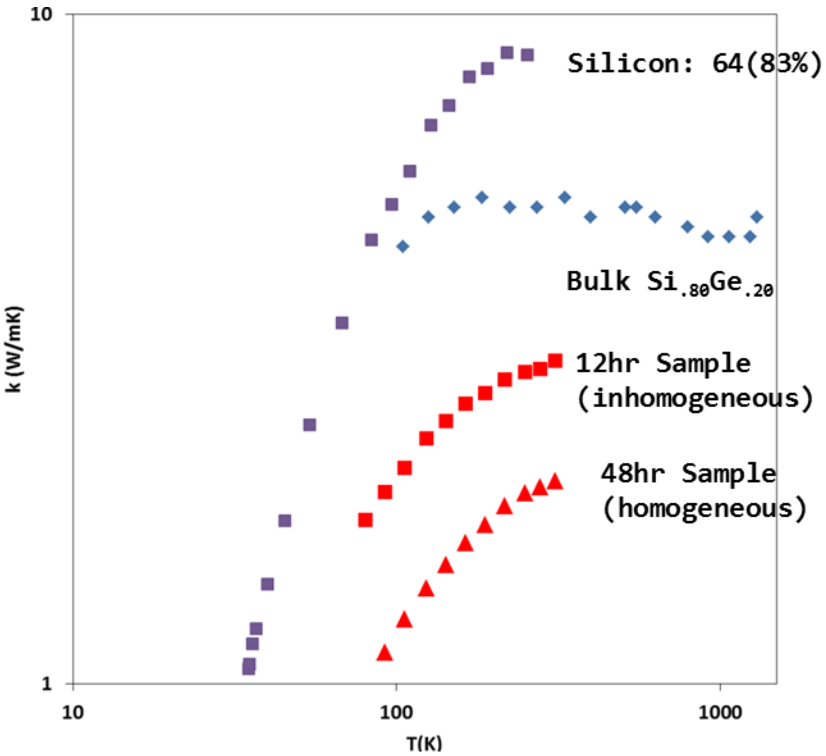

Figure 5.8: Thermal conductivity plot of the 12hr and 48hr samples compared to the 64(83%) sample from chapter 4 and a bulk Silicon Germanium alloy [11] found in literature

.

5.7 References

[1] W. Kim et al. Phys. Rev. Lett **96**, 045901 (2006) 1-4

[2] H. Stohr et al. Anorg. Allgem. Chem. **241** (1954) 305

[3] M. Levinshtein, S. L. Rumyanstev, M. S. Shur, *Properties of Advanced Semiconductor Materials,* John Wiley & Sons, New York, (2001) pg. 178

[4] G. Joshi et al. Nano Lett. **8** (2008) 4670-4674

[5] H. Lee et al. J. Appl. Phys. **107, 094308** (2010) 1-6

[6] X. W. Wang et al. Appl. Phys. Lett. **93** (2008) 1-3

[7] G. Zhu et al. Phys. Rev. Lett. **102** (2009) 1-4

[8] X. Pixius et al. Scripta Metall. et. Mater. **33** (1995) 407-413

[9] D.B. Cullity, S.R. Stock, *Elements of X-ray Diffraction 3rd Edition,* Prentice Hall, New Jersey, (2001)

[10] C.C. Koch, Annu. Rev. Mater. Sci **19** (1989) 121-143

[11] S.M. Lee et al. Appl. Phys. Lett. **70**, 2957 (1997)

Chapter 6: Grain Size Distribution- Effects on Thermal Conductivity

6.1 Background

Chapter 4 showed that the grain size of nano-structured thermoelectric materials significantly affects thermal conductivity. The model described in that chapter shows both the grain size and the phonon frequency alters the mean free path of the phonons. When using this model to predict the thermal conductivity of real materials, a single average grain size is assumed for the entire sample. While this approach was shown to predict the thermal conductivity of the Silicon samples accurately, real powders and real samples have a grain size distribution that can range from a narrow distribution to a wide range of grain sizes as shown in figure 6.1a. The histograms of the 76(99%) sample and the 550(99%) sample are shown in figures 6.1a and 6.1b respectively. The sample with an average grain size of 76 nm shows a very narrow distribution of grain sizes ranging from 40 to 165 nm. The larger grained sample produced with a different powder has a much wider distribution between 147 and 1709 nm. This difference shows that the grain size can vary significantly even in commercial powders.

Several reports in literature have cited grain size distribution as being a potential mechanism for decreasing the thermal conductivity of materials beyond the effects of reducing grain size alone [1-3]. The explanation given is that a wide grain size distribution will affect phonon distribution differently due to phonons with varying MFPs. Though being cited as an explanation for unexpectedly low thermal conductivity, the effects of grain size distribution have not been systematically investigated. Manipulating the distribution of grain sizes to maintain the overall average grain size of a powder would present significant difficulties, but this chapter explores a novel group of materials with a bimodal grain size distribution as shown in figure 6.2.

As shown in chapter 4, the thermal conductivity of the coarse material is significantly higher than that of the nano-material. In a bimodal grain size material, the phonon MFP will be truncated due to grain boundary scattering in the nano-region, but will be longer in the coarse region. An illustration of this effect is shown in figure 6.3. If the thermal conductivity of the sample is decreased with changes to the grain size distribution, this would support the theory that additional grain sizes scatter additional phonons. While microstructure has been shown to affect the thermal conductivity of these materials, there are currently no systematic studies on the effects of changing the grain size distribution in regards to the thermal conductivity. The study shown in this chapter attempts to determine if this material property will have a direct relation to the changing microstructure or an indirect relation such as a percolation type behavior.

6.2 Procedure

The Silicon powders used to produce all of the samples in this study are the same powders used in Chapter 4: a nano-grained commercial powder with little agglomeration and a commercial powder that is heavily agglomerated with relatively large grain sizes. Five samples were made with a mixture of these two powders so that the concentration by weight of the samples is 0%, 25%, 50%, and 100% coarse powder. The fully dense nano sample (76(99%)) and the fully dense coarse sample (550(99%)) from chapter 4 are used in this study as the 0% and 100% samples respectively. These samples were previously known to have grain sizes between 40-165 nm and 147-1709 nm respectively from the previous study. The three samples produced for this study were mixed via hand milling as described in chapter 2 and were densified via the CAPAD technique at 1200^{o}C with a pressure of 106 MPa and a hold time at temperature of 10 minutes. All of the samples here were produced using the graphite foil technique described in chapter 3 and were densified under vacuum.

Due to the difficulties in resolving both the coarse and the nano grains in a sample using a single SEM micrograph, fracture surfaces of both regions were analyzed separately for each sample. In order to determine the grain size distribution of a total sample, the grain size data of the two regions were treated separately and the data was added together as described here. Table 6.1 describes all of the variables used in the calculations described below and can be used to systematically follow the calculations step by step.

For each grain size regime (coarse and nano), grains were measured and histograms were made with bin widths of 10 nanometers. For each histogram, the number of counts in each grain size range were normalized to the total number of grains counted in each regime as shown in equation 6.1.

$$x_{bin}^{c} = \frac{N_{bin}^{c}}{N_{tot}^{c}} \qquad\qquad x_{bin}^{n} = \frac{N_{bin}^{n}}{N_{tot}^{n}} \tag{6.1}$$

The number of counts in each grain size range for the nano and coarse regimes are represented as N_{bin}^{n} and N_{bin}^{c} respectively while the total number of counts in each powder regime are represented as N_{tot}^{n} and N_{tot}^{c} respectively. The resulting normalized data, x_{bin}^{c} and x_{bin}^{n} for the coarse and nano regimes respectively, produces histograms in which the data represents the weighted contribution of each grain size to their respective regimes. The values in each bin of these histograms was weighted by the volume ratios of the coarse and nano powders contained in each sample. These weighted values were then added to produce a histogram representative of the entire sample as shown in equation 6.2

$$(x_{bin}^{c} \times \phi_c) + (x_{bin}^{n} \times \phi_n) = X_{bin}^{tot} \tag{6.2}$$

In which the volume ratios of the coarse and the nano powders in the samples is represented by ϕ_c and ϕ_n respectively.

The thermal diffusivity of the samples was measured by Dr. Sabah Bux at the Jet Propulsion Laboratory (Burbank, CA) by utilizing the laser flash method described in chapter 3 and the room temperature values are compared to a simple linear model. The model was calculated using the rule of mixtures with the room temperature thermal conductivities of the pure nano and the pure coarse powders as shown in equation (6.3). The thermal conductivity values utilized in these calculations were the room temperature values measured for the 76(99%) and 550(99%) samples discussed in chapter 4 and are represented below as k_n and k_c respectively.

$$(G_c \times k_c) + (G_n \times k_n) = \kappa_{ROM} \tag{6.3}$$

In which G_c and G_n are the fraction of the samples comprised of coarse and nano grains respectively and κ_{ROM} is the predicted rule of mixtures based thermal conductivity. The measured values used for k_n and k_c were 28.38 W/m-K and 81.9 W/m-K respectively. This linear prediction is shown by the black line in figure 6.8. In order to estimate the relative fraction of coarse grains and nano grains in each sample, the X_{bin}^{tot} histograms were used. In each regime, the height of the maximum peaks was used to represent the fraction of coarse grains and nano grains contained within the sample. Based upon the histograms of the 0% and 100% coarse samples, the nano regime was considered to be any grain size up to 300 nm and the coarse regime was considered to be any grain larger. These relative ratios in combination with equation (6.3) were used to predict the rule of mixture estimates for the room temperature thermal conductivity of each of the samples investigated here.

6.3 Results

The density of each of the samples used in this study was measured using the Archimedes technique and they all showed a density of 99% or higher. The SEM micrograph shown in figure 6.4 shows a polished surface of the sample composed of equal amounts of both powders (the 50% coarse sample). This micrograph shows that the densified samples are fully dense samples in which large agglomerates of the coarse powder are surrounded by regions or “valleys” of the nano-material. Closer inspection of the interfaces between these regions does not indicate that there is a gradual decrease in the grain size between the coarse material and the nano-material, but rather the transition is sudden, with a well-defined boundary between the two regions.

The Histograms shown in figure 6.5a and b show the calculated grain size distribution of each sample. These histograms show that as the concentration of coarse powder is increased in the samples, the grain size distributions become more widely distributed across a larger spectrum of grain sizes, but rather than making a gradual transition of a single maximum into larger grain sizes, the microstructure remains confined to the two distributions seen in the starting powders.

The plot in figure 6.6 shows the room temperature thermal conductivities of the 76(99%) sample and the 556(99%) sample, though the thermal conductivity of these samples were not measured in the high temperature range due to the unavailability of the samples. The thermal conductivity of the remaining three samples used in this study are shown along with the values for single crystal Silicon obtained from literature for comparison. This data shows that while all of the data for the mixed samples are higher than that of the 0% coarse sample and lower than that of the 100% coarse sample, the values of the 25% and 50% coarse powder only differ from one another by 10% and the values of the 50% and the 75% samples differ by 25%. This non-linear variation is shown for the room temperature values of each of the samples in figure 6.7. This graph shows that there is little change in the room temperature thermal conductivity for the 25-50% coarse samples, but the conductivity values change significantly as the concentration of the coarse powder is further increased. An initial increase in thermal conductivity is seen between the 0% and 25% samples. The estimated room temperature thermal conductivity calculated using equation (6.3) is shown in figures 6.7 and 6.8. Figure 6.8 compares this model to the plot of the thermal conductivity as a function of % of the total sample comprised of coarse grains. The experimental data closely follows the linear rule of mixtures estimate with the largest deviation being only 6%.

6.4 Discussion

Despite the fact that the 100% course grained sample has a significantly wider grain size distribution than that of the 0% sample, the sharp interface seen between the nano and the coarse grained regions of the mixed samples allows for the investigation of the effects of a bimodal sample like the one shown in figure 6.2 rather than a sample with a single wide distribution like that shown in figure 6.1a. The grain size distributions of the samples shown in figure 6.5 indicate that as the contribution of the course material increases, the nano regime becomes less influential. Though the relative height of the peaks in the two regimes do not appear to be comparable in the 50% coarse sample, the percent of the sample that is comprised of each type of powder is equal to their percent by volume. The discrepancy in the relative peak heights are due to a number of factors. Because the grains in the coarse regions are so much larger than those in the nano regions, the number of coarse grains in a certain volume is significantly fewer than the number of grains in an equal volume of the nano-material. Additionally, because the width of the distributions differs considerably, the number of counts in a particular range of grain sizes will also differ between the two regions. Because of this, the counts of the nano regime appear to significantly dominate the overall counts in the samples for all the samples besides the 75% and 100% coarse materials.

The non-linearity of figure 6.7 and the linearity of figure 6.8 along with the accuracy of the predicted thermal conductivity values show that the thermal conductivity is, to a very close approximation, a function of the number of nano-grains contained within a sample rather than the volumetric composition of the sample. This direct correlation between the thermal conductivity of the samples and the number of nano-grains contained within indicates that very wide grain size distributions could potentially lower the overall conductivity of a sample due to the presence of features significantly smaller than the average grain size. The data shown in figures 6.7 and 6.8, however, indicate that a significant change in thermal conductivity would require a significantly large change in the number of nano-features within a material. Such a change in microstructure would likely result in a decrease in the overall average grain size of the material, and is not likely the cause of thermal conductivity being significantly lower than the predicted value in most studies. Further, the direct correlation with the rule of mixtures indicates that different phonons with differing wavelengths are not filtered by grains of specific sizes, but rather the mean free path of the phonons are altered as shown in figure 6.3. It is more likely that unexpectedly low thermal conductivity values reported in published studies are due to the presence of other nano-features such as porosity or regions of inhomogeneity as discussed in chapters 4 and 5.

6.5 Summary

The thermal conductivity as a function of grain size distribution was explored for samples created with varying concentrations of Silicon powders with two different microstructures. It was shown that the thermal conductivity of these pure silicon samples was directly correlated to the number of nano-grains contained within the material. It is concluded that a wide grain size distribution is not likely the reason for unexpected thermal conductivity values in most reports, but rather the result of the inclusion of other phonon scattering mechanisms.

6.6 Figures

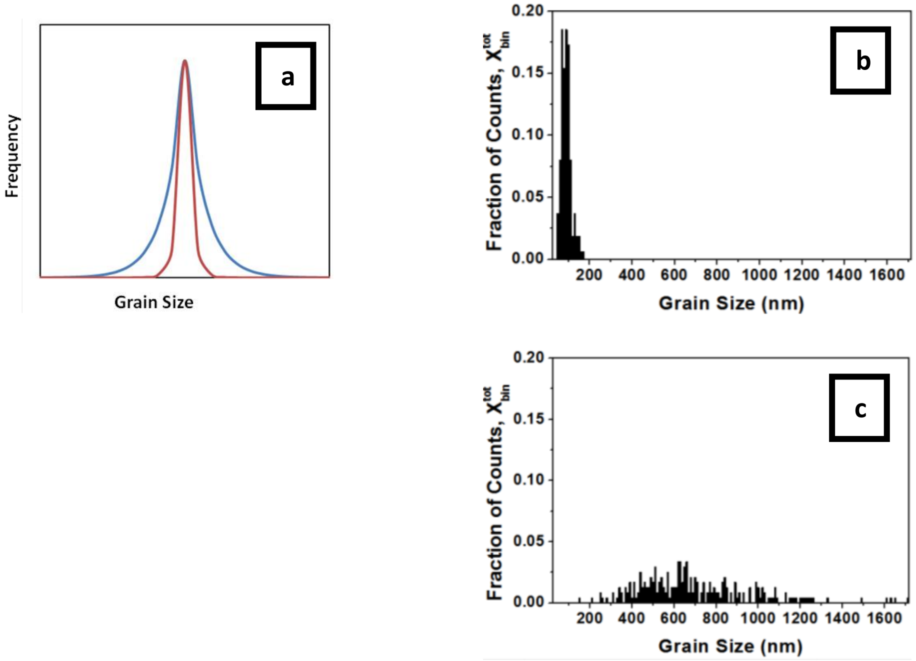

Figure 6.1: Schematic showing the difference between a wide (blue) and narrow (red) grain size distribution (a) and measured distributions of two commercial Silicon powders: a nano-powder provided by Lockheed Martin (a) and a large grained +325 mesh powder from Alpha Aesar (c).

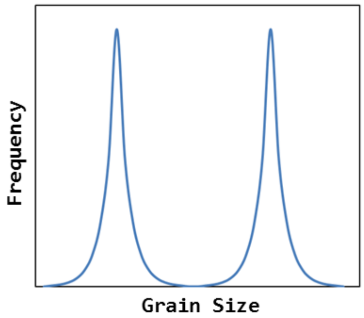

Figure 6.2: A schematic of a theoretical bimodal grain size distribution.

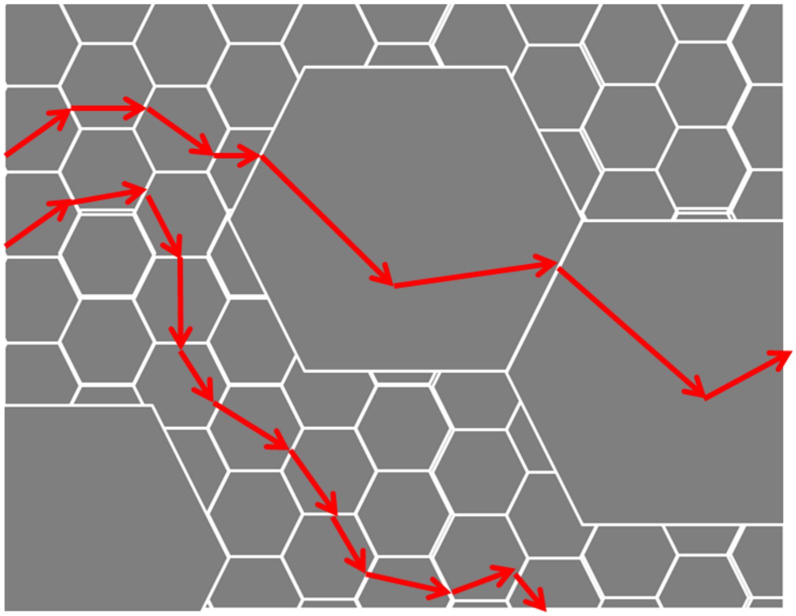

Figure 6.3: Schematic showing the behavior of phonons in a sample with varying grain size.

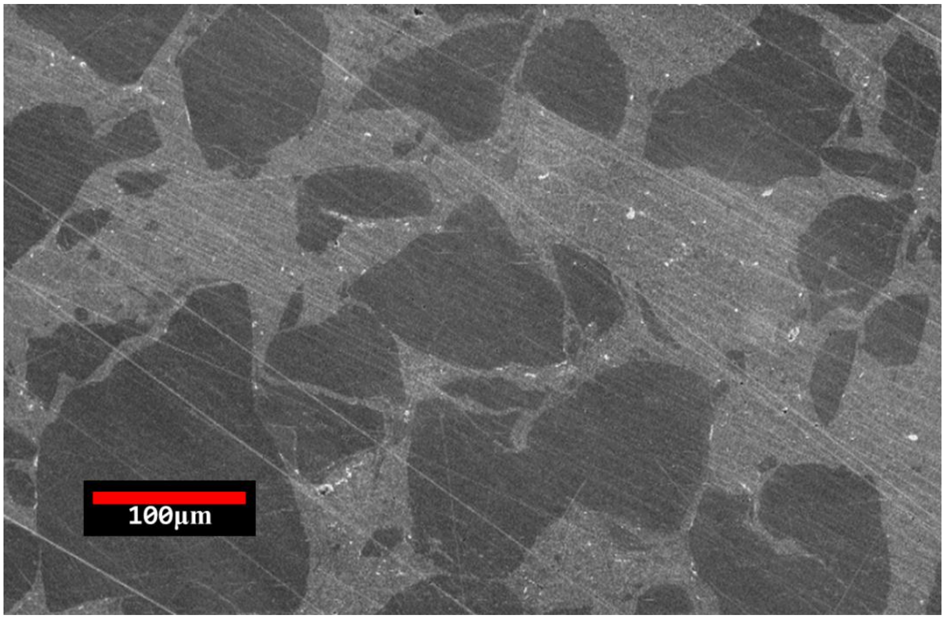

Figure 6.4: Secondary Electron Micrograph of a polished surface of the 50% coarse sample showing large coarse grained regions (dark regions) surrounded by regions of nano-grained material (lighter regions).

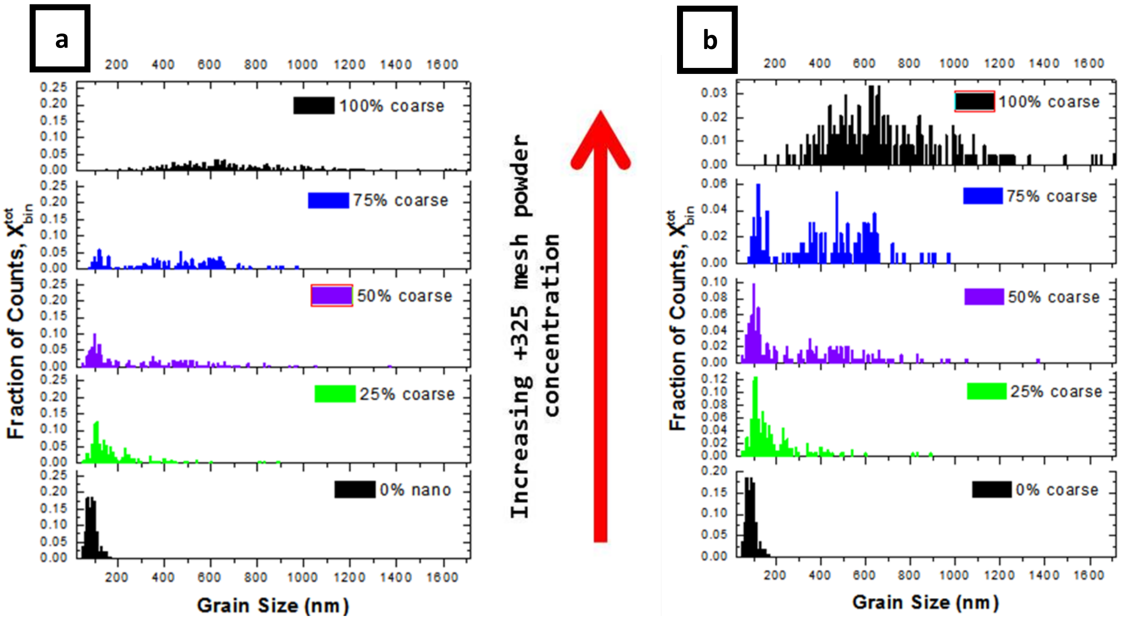

Figure 6.5: Distribution profiles of samples with varying concentrations of coarse Silicon material. The data is shown with the axes on the same scale for comparison (a) as well as the same data with the axes adjusted (b) to make it easier to compare the relative heights of the distribution peaks in the samples.

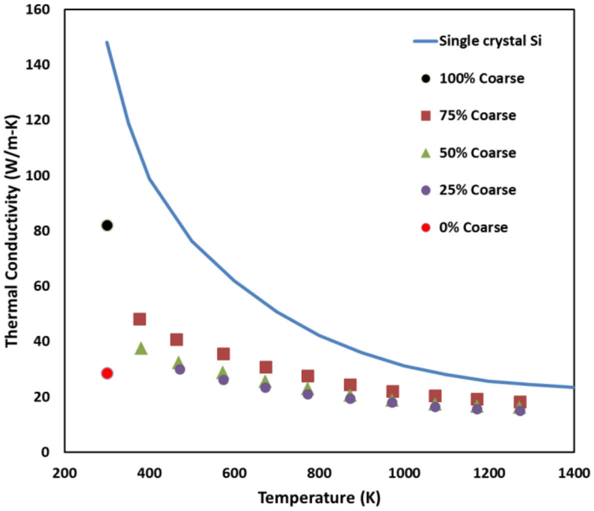

Figure 6.6: Plot of the thermal conductivity of the grain size distribution samples above room temperature. For comparison, the thermal conductivity of single crystal Silicon is shown (solid line).

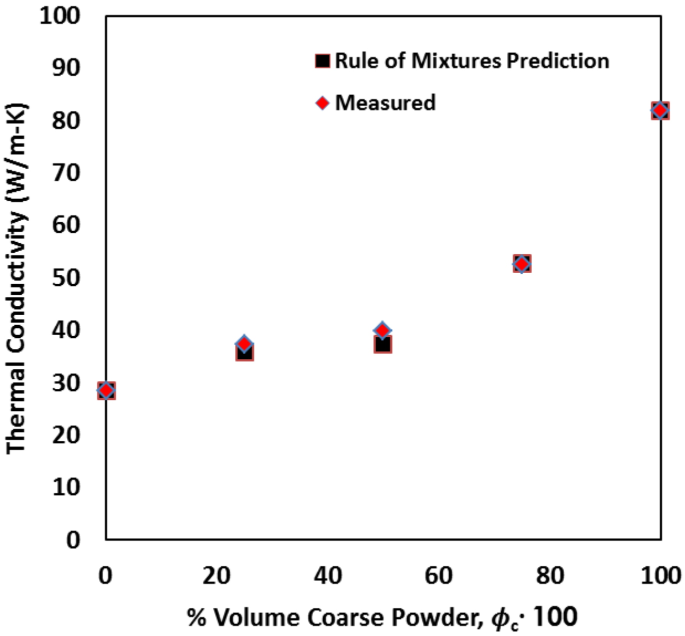

Figure 6.7: Plot of predicted and measured room temperature thermal conductivity vs. % by volume coarse powder concentration. The Predicted values (calculated with equation (6.3) are all within 6% of the measured values.

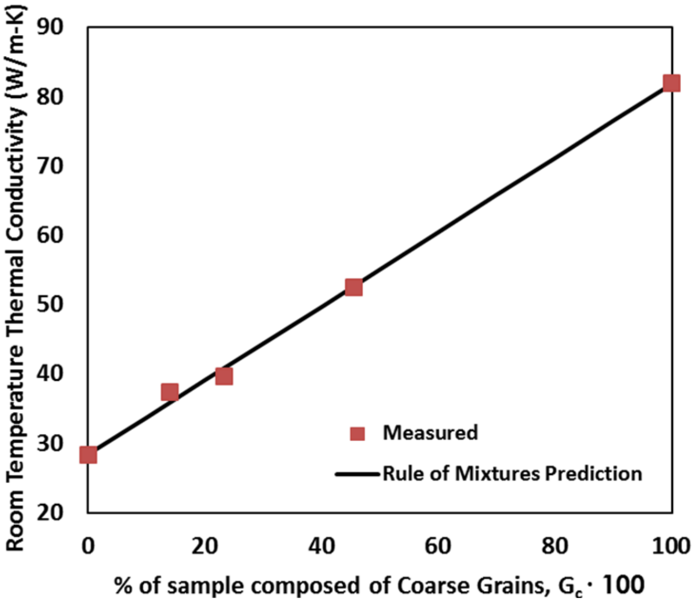

Figure 6.8: Plot of the room temperature thermal conductivity vs. the % concentration of coarse grains contained within the sample. The data conforms to the linear rule of mixtures model (equation 6.3) within 6%.

Symbol	Description	Calculation or Value
N_{bin}^{c}	# of grains counted with a grain size within histogram bin for coarse region of sample	
N_{bin}^{n}	# of grains counted with a grain size within histogram bin for nano region of sample	
N_{tot}^{n}	Total # of grains counted in coarse region	
N_{tot}^{n}	Total # of grains counted in nano region	
x_{bin}^{c}	# fraction of grains in coarse region that fall within bin for coarse histogram	$x_{bin}^{c} = \frac{N_{bin}^{c}}{N_{tot}^{c}}$ **eqn (6.1)**
x_{bin}^{n}	# fraction of grains in nano region that fall within bin for nano histogram	$x_{bin}^{n} = \frac{N_{bin}^{n}}{N_{tot}^{n}}$ **eqn (6.1)**
ϕ_c	Volume fraction of coarse Silicon in sample	
ϕ_n	Volume fraction of nano Silicon in sample	
X_{bin}^{tot}	# fraction of total grains in sample with grain size within bin range	$(x_{bin}^{c} \times \phi_c) + (x_{bin}^{n} \times \phi_n)$ **eqn (6.2)**
X_{max}^{c}	Maximum bin height measured above 300nm (coarse region)	
X_{max}^{n}	Maximum bin height measured below 300nm (nano region)	
G_c	# fraction of coarse grains in total sample	$\frac{X_{max}^{c}}{X_{max}^{c} + X_{max}^{n}}$
G_n	# fraction of nano grain in total sample	$\frac{X_{max}^{n}}{X_{max}^{c} + X_{max}^{n}}$
k_n	Room temperature thermal conductivity measured in chapter 4 for 550(99%) sample (0% coarse)	28.4 $\frac{W}{m-K}$
k_c	Room temperature thermal conductivity measured in chapter 4 for 76(99%) sample (100% coarse)	81.9 $\frac{W}{m-K}$
K_{ROM}	Rule of mixtures prediction for room temperature thermal conductivity of sample	$(G_c \times k_c) + (G_n \times k_n)$ **eqn (6.3)**

Table 6.1: Variables and calculations used to calculate the sample histograms and rule of mixtures thermal conductivity model as described in section 4.2. Superscript and subscript lower-case “c” and “n” represent calculations performed while focusing on the coarse and nano regions of the sample separately.

6.7 References

[1] Y. Lan et al. Nano Lett. **9** (2009) 1419-1422

[2] G. Joshi et al. Nano Lett. **8** (2008) 4670-4674

[3] S. Bux et al. Adv. Func. Mat. **19** (2009) 2445-2452